REPORT DOCUMENTATION PAGE

Form Approved
OMB No. 0704-0188

1. REPORT DATE	2. REPORT TYPE	3. DATES COVERED *(From - To)*
12 December 2019	Technical Paper	22 October 2019 - 31 December 2019

4. TITLE AND SUBTITLE
Elucidating the phenomena that govern reaction dynamics in assembled nanostructured energetic materials at scales relevant to munitions and propellants

5a. CONTRACT NUMBER

5b. GRANT NUMBER

5c. PROGRAM ELEMENT NUMBER

6. AUTHOR(S)
Jerry A. Boatz

5d. PROJECT NUMBER

5e. TASK NUMBER

5f. WORK UNIT NUMBER
Q188

7. PERFORMING ORGANIZATION NAME(S) AND ADDRESS(ES)
Air Force Research Laboratory (AFMC)
AFRL/RQRP
10 E. Saturn Blvd.
Edwards AFB, CA 93524-7680

8. PERFORMING ORGANIZATION REPORT NUMBER

9. SPONSORING/MONITORING AGENCY NAME(S) AND ADDRESS(ES)

Air Force Research Laboratory (AFMC)
AFRL/RQR
5 Pollux Drive
Edwards AFB, CA 93524-7048

10. SPONSOR/MONITOR'S ACRONYM(S)

11. SPONSOR/MONITOR'S REPORT NUMBER(S)

AFRL-RQ-ED-TP-2019-352

12. DISTRIBUTION/AVAILABILITY STATEMENT
Distribution Statement A: Approved for Public Release; Distribution is Unlimited. PA Clearance Number: 19574 Clearance Date: 09 December 2019.

13. SUPPLEMENTARY NOTES
AFOSR Report. The U.S. Government is joint author of the work and has the right to use, modify, reproduce, release, perform, display, or disclose the work.

14. ABSTRACT
The overall objective of this LRIR is to make, model and measure materials that can be safely assessed for high energy density and fast reaction rates (> 1 km/s). The overarching goal is to synthesize, characterize and more accurately predict potential candidate materials such as energetic core shell nanoclusters, with energy densities exceeding that of organic explosives, to determine their role in existing and future Air Force munitions and propellants. Regarding specifically the theoretical/computational component of this LRIR, the primary objectives are to predict key properties of core-shell-nanoclusters, including, for example, intrinsic stabilities, fundamental nature of the interactions between core-shell layers, and kinetic stabilities of oxidizer-coated-nanoclusters (i.e, nano-thermites.) Due to the frequent use of aluminum in explosive and propellants, core-shell nanoclusters containing aluminum are of primary interest. Specific computational efforts described herein include (a) structure and energetics of Al coreshell nanoclusters (b) the possibility of inversion of such core-shell species and (c) the oxidation of aluminum nanoclusters. In addition, a series of calculations designed to investigate the fundamental limits of chemical energy storage based upon chemical bond lengths and bond energies is summarized.

15. SUBJECT TERMS
N/A

16. SECURITY CLASSIFICATION OF:			17. LIMITATION OF ABSTRACT	18. NUMBER OF PAGES	19a. NAME OF RESPONSIBLE PERSON
a. REPORT	b. ABSTRACT	c. THIS PAGE			Jerry A. Boatz
Unclassified	Unclassified	Unclassified	SAR	41	19b. TELEPHONE NUMBER *(Include area code)* N/A

AFOSR LRIR Number: 17RQCOR451

LRIR Title: Elucidating the phenomena that govern reaction dynamics in assembled nanostructured energetic materials at scales relevant to munitions and propellants

Reporting Period: 1 Oct 2016 – 30 Sep 2019

Laboratory Task Manager: Jerry A. Boatz

Project Officer: Michael Berman

1. Research Objectives

The overall objective of this LRIR is to make, model and measure materials that can be safely assessed for high energy density and fast reaction rates (> 1 km/s). The overarching goal is to synthesize, characterize and more accurately predict potential candidate materials such as energetic core shell nanoclusters, with energy densities exceeding that of organic explosives, to determine their role in existing and future Air Force munitions and propellants. Regarding specifically the theoretical/computational component of this LRIR, the primary objectives are to predict key properties of core-shell-nanoclusters, including, for example, intrinsic stabilities, fundamental nature of the interactions between core-shell layers, and kinetic stabilities of oxidizer-coated-nanoclusters (i.e, nano-thermites.) Due to the frequent use of aluminum in explosive and propellants, core-shell nanoclusters containing aluminum are of primary interest. Specific computational efforts described herein include (a) structure and energetics of Al core-shell nanoclusters (b) the possibility of inversion of such core-shell species and (c) the oxidation of aluminum nanoclusters. In addition, a series of calculations designed to investigate the fundamental limits of chemical energy storage based upon chemical bond lengths and bond energies is summarized.

Core-shell Al Nanoclusters

Core-Shell Formation

In connection with experimental studies of Al core-shell nanocluster formation conducted by our collaborators at AFRL/RW (Eglin AFB), there is a critical need for a fundamental understanding of the core-shell nanocluster formation processes and the nature of the chemical and physical interactions at the core-shell interface. Nanoclusters are synthesized via helium droplet mediated deposition (HDMD) methods in which synthesis occurs via clustering of atoms or molecules within the interior of helium droplets, as described in detail elsewhere[1-9]. Briefly, ultracold helium droplets are generated via supersonic expansion and sequentially passed

through multiple pickup cells, each of which can contain an atomic or molecular species in the vapor phase. As individual atoms or molecules are trapped by the helium droplet, they coalesce in the droplet interior, leading to the formation of "core" nanoclusters. If the thus-formed nanocluster-seeded helium droplets subsequently pass through a second pickup cell containing a different atomic or molecular species, the "shell" layer can be formed by a similar mechanism. As captured species begin to coalesce, energy is released and dissipated via evaporative cooling of the surrounding helium droplet. Therefore, it is important to understand the bonding characteristics, binding energies, and stabilities of these metallic clusters to help characterize these nanoclusters as well as understand their formation in these experiments. Aluminum is investigated as it is a relevant energetic material in conjunction with gold, copper, and silicon as they are well studied and relatively experimentally friendly materials to utilize in HDMD.

Based on previous work with boron and aluminum clusters[10-13] it was determined that use of the Al_{80} cluster would be of an appropriate size and computationally feasible and therefore is chosen as the initial cluster size to be used in these studies. For a cluster of this size, density functional theory (DFT) methods are the most suitable. Therefore, critical benchmarks of several DFT functionals for the relevant dimers present in Al/Cu, Al/Au, and Al/Si core shell systems were performed. The functionals that were investigated are B3LYP[14-16], B3PW91[14, 17-21] and PBE0[22, 23]. These results, both geometries and energetics, were compared to second order perturbation (MP2)[24-26] and coupled cluster (CR-CC(2,3))[27, 28] methods, all using the SBKJC basis set[29, 30] with the addition of polarization and diffuse functions for Al and Si, alongside available experimental data, as is seen in Table 1. All calculations are done utilizing the GAMESS suite of programs[31, 32].

Table 1. Geometries and Binding Energies (kcal mol^{-1}) of Al, Au, Cu, and Si dimers

	B3LYP		B3PW91		PBE0		MP2		CR-CC(2,3)		EXP	
	R(Å)	B. E.	R(Å)	B. E.	R(Å)	B. E.	R(Å)	B. E.	R(Å)	B. E.	R(Å)	B. E.
Al_2	2.782	29.6	2.770	32.8	2.766	33.8	2.717	26.2	2.716	28.3	2.701[33]	30.9[34]
Cu_2	2.277	42.6	2.263	41.8	2.268	42.0	2.287	37.9	2.295	43.1	2.22[35]	
Au_2	2.574	44.2	2.548	45.0	2.544	45.7	2.561	43.2	2.568	46.1		
Si_2	2.296	69.8	2.293	72.2	2.288	72.4	2.266	59.0	2.282	60.2	2.246[36]	74.1[36]
AlCu	2.408	49.4	2.404	48.8	2.414	47.9	2.394	42.4	2.409	47.4		
AlAu	2.414	71.8	2.404	72.4	2.405	71.8	2.404	64.8	2.414	70.2		
SiAl	2.472	31.4	2.463	32.6	2.460	32.9	2.427	23.2	2.459	26.9		

The DFT diatomic bond lengths are generally in satisfactory agreement with predictions at the coupled cluster level, and with the available experimental data. The largest difference is observed in Al_2, where the B3LYP bond length of 2.782 Å is approximately 0.06 Å larger than the CR-CC(2,3) value of 2.716 Å, and 0.08 Å larger than the experimental bond length of 2.701 Å. In general, for the homonuclear diatomics, the DFT methods yield slightly larger bond lengths than experiment.

The DFT binding energies are typically within 5 kcal mol^{-1} of the CR-CC(2,3) values. An exception is Si_2, where the DFT binding energies are 10-12 kcal mol^{-1} larger than the coupled cluster predicted value of 60.2 kcal mol^{-1}. However, the DFT binding energies of Si_2 are in excellent agreement with the experimental value of 74.1 kcal mol^{-1}, which CR-CC (2,3) underestimates by 14 kcal mol^{-1}.

Al_{80} clusters were optimized using all three functionals, as seen in Figure 1 alongside the atomization energy, the difference in energy between the optimized cluster and the sum of 80 Al atoms. The B3LYP atomization energy of 4063.4 kcal mol^{-1} is considerably smaller than B3PW91 (4861.3 kcal mol^{-1}) and PBE0 (5137.5 kcal mol^{-1}). This is in part due to the differences in Al-Al binding energies seen in the dimer calculations. It should be noted that from the dimer calculations shown above that B3LYP provides an Al-Al binding energy that is in better agreement with both the coupled cluster and experimental energies than the other functionals.

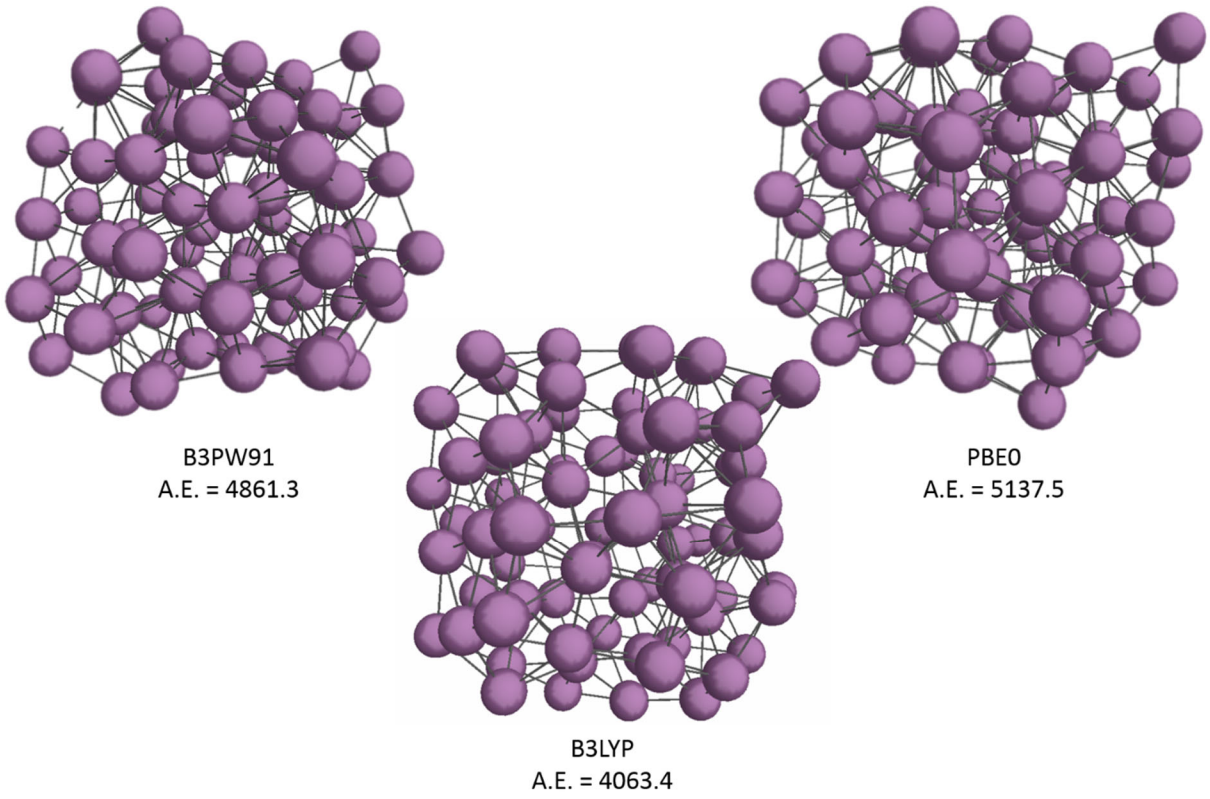

Figure 1. DFT/SBKJC optimized structures of Al_{80}, using the indicated functional. Atomization energies are in kcal mol^{-1}.

The possibility for aluminum clusters to coalesce after formation within the He droplet and deposited onto a substrate is of interest and importance. To investigate this, the potential energy surface of an Al_{30} cluster coming into contact with an Al_{50} cluster was calculated, as illustrated in Figure 2. This was done by starting with the fully optimized Al_{30} and Al_{50} structures, initially separated by a distance R=20 Å between a specific pair of interior "anchor"

atoms, one located in each of the component clusters. A series of constrained optimizations was performed in which R was held fixed while the remaining structural degrees of freedom were optimized. The constrained distance R was then reduced in steps of 1 Å by rigidly shifting all of the atoms in the Al_{30} cluster along the constraint axis toward Al_{50}, and then reoptimizing.

The energy trace of this series of constrained optimizations is shown in Figure 2. The energy as a function of constraint distance R is essentially flat until R=13 Å, at which point the energy begins to sharply drop. The structure at R=12 Å shows three inter-cluster bonds between 5 atoms, with a binding energy of 51 kcal mol^{-1}. Not surprisingly, the energy curve suggests the lack of any significant barrier for recombination of the Al_{30} and Al_{50} clusters. This suggests that coalescence of deposited aluminum nanoclusters formed in the helium droplet experiments can readily occur, provided that the deposited clusters are sufficiently close together and that the cluster surfaces are pristine; e.g., no oxide layer is present which might inhibit cluster recombination.

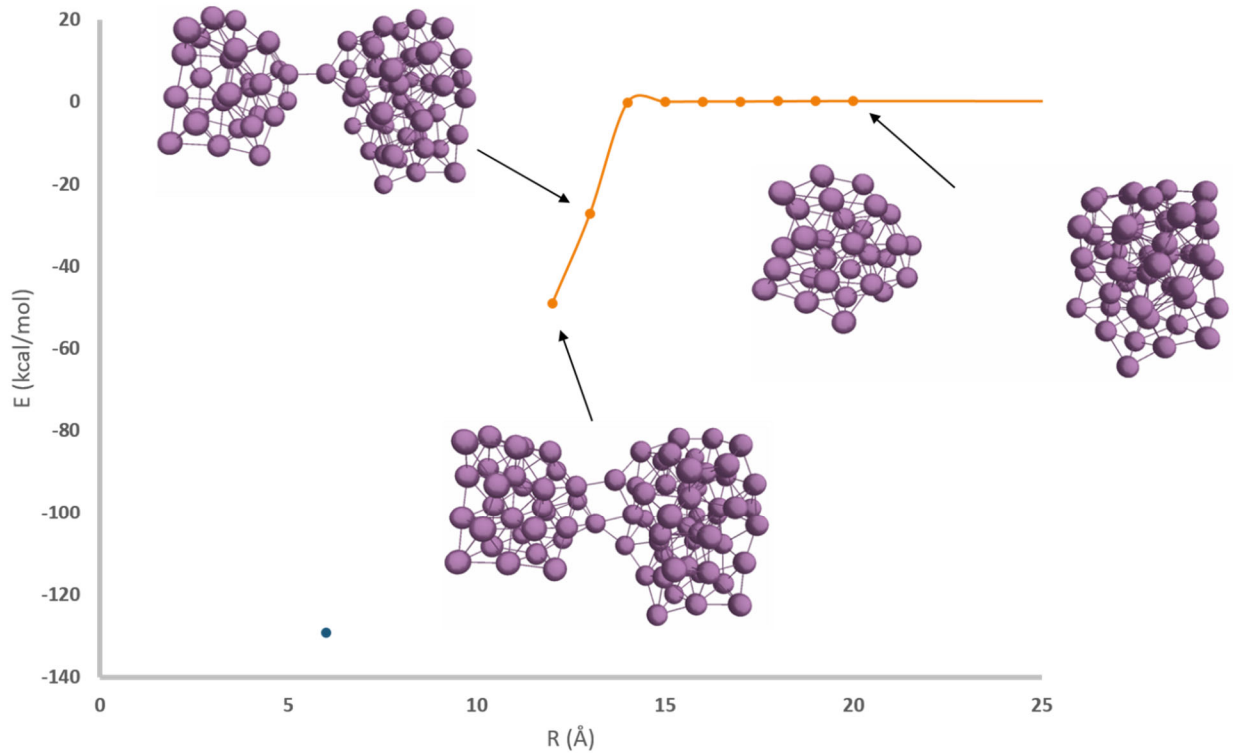

Figure 2. Potential energy surface (PES) (orange) of the coalescence of an Al_{30} cluster and Al_{50} cluster, calculated at the B3LYP/SBKJC level of theory. The blue point indicates the relative energy of the fully optimized Al_{80} cluster.

In order to determine the ability of gold, copper, or silicon to create a shell around an Al nanocluster, two single atoms adsorbing to the surface of an Al_{80} cluster was investigated. Two limiting cases of adsorption onto the surface were investigated, one in which the atoms are on

opposite sides of the cluster, and one in where they are adjacent to each other. All of the bimetallic clusters M_2Al_{80} (M=Cu, Au or Si) have been optimized using the functionals and basis set mentioned above. The optimized Al_{80} clusters shown in Figure 1 above were used as initial Al_{80} structures, with two Au, Cu, or Si atoms placed on the surface, followed by reoptimization of the entire M_2Al_{80} cluster.

The Al/Au clusters were investigated first, having two gold atoms deposited onto an Al_{80} surface on opposing ends of the cluster as seen in Figure 3. The gold atoms bind strongly to the surface of the Al cluster, with binding energies of 147.3(B3LYP), 166.0(B3PW91), and 168.9(PBE0) kcal mol^{-1}, relative to the sum of the energies of separated Al_{80} + 2Au. Each of the individual gold atoms is strongly chemisorbed onto the Al cluster surface with the apparent formation of at least three Au-Al bonds. In trying to determine the ability of gold to fully coat the surface of an Al cluster yielding a core-shell nanocluster, it is imperative to understand the ability of neighboring gold atoms to adhere to the surface. This was investigated by taking the optimized $Al_{80}Au_2$ structures shown in Figure 3, moving one of the gold atoms next to the other, and then reoptimizing, with the fully optimized structures shown in Figure 4.

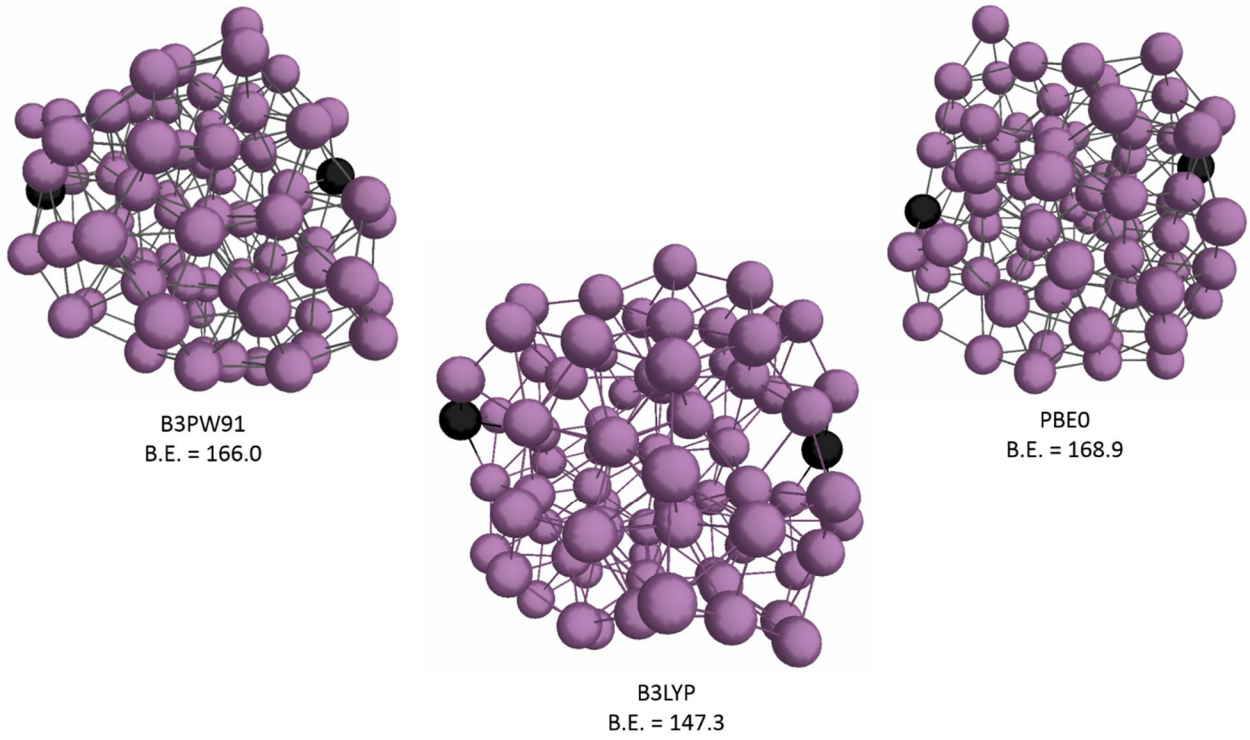

Figure 3. $Al_{80}{\cdot}Au_2$ optimized structures with gold atoms on opposite side of the cluster. Binding energies are in kcal mol^{-1}.

Similar to the $Al_{80}{\cdot}Au_2$ clusters shown in Figure 3, when the gold atoms are adjacent to each other on the Al_{80} surface, they appear to bond well to the surface, with the gold atoms being associated with at least 3 Al atoms on the surface and yielding binding energies of 132.5, 143.8 and 157.3 kcal mol^{-1} for B3PW91, B3LYP and PBE0 functionals respectively. However, all

three DFT methods predict the neighboring gold atoms (Figure 4) to have lower binding energies relative to separated gold atoms on the Al_{80} surface (Figure 3.) This is consistent with the relative bond energies of the Au_2 and Al-Au dimers. As shown in Table 1, the predicted bond energies of Au_2 range from 42 to 46.1 kcal mol^{-1}, whereas the Al-Au bond energies range from 64.8 to 72.4 kcal mol^{-1}. Due to retention of an Au-Au interaction in the chemisorbed Au dimer, the residual Al-Au bonding interactions are expected to be weaker than those present in the case of separated chemisorbed Au atoms, where only Al-Au binding is present and the (weaker) Au-Au interactions are absent. It should be noted that in the case of adjacent Au atoms on the Al_{80} surface (Figure 4), the Au-Au bond length increases relative to the bare Au_2 diatom. Specifically, the Au-Au distance is 2.850, 2.805, and 4.162 Å in the B3PW91, PBE0, and B3LYP structures, respectively. In fact, for B3LYP the "adjacent" Au atoms have essentially dissociated to form separated chemisorbed Au atoms. This is consistent with the similarity in atomization energies of this structure (143.8 kcal mol^{-1}, Figure 4) with the corresponding B3LYP structure in which the Au atoms are on opposite sides of Al_{80} (147.3 kcal mol^{-1}, Figure 3.)

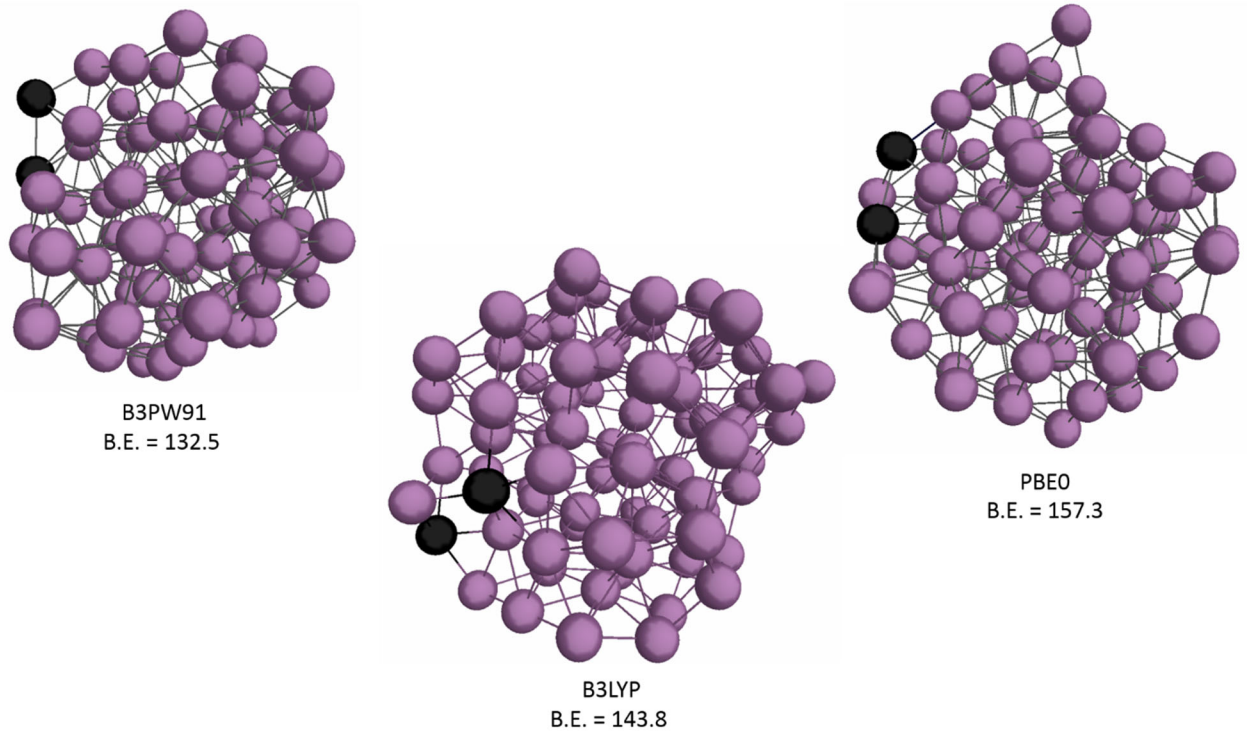

Figure 4. Al_{80}·Au_2 optimized structures with adjacent gold atoms on the cluster surface. Binding energies are in kcal mol^{-1}.

A complementary analysis of the binding of two copper atoms on the surface of Al_{80} reveals similar behavior to the $Al_{80}Au_2$ clusters. Specifically, separated Cu atoms on the surface appear to form multiple bonds to the Al_{80} surface, as illustrated in Figure 5. The same is true for the Cu_2 dimer on the Al_{80} surface, shown in Figure 6. As in the case of Au_2 dimers on the Al_{80} surface, the Cu-Cu bond lengths are significantly longer relative to the bare Cu_2 dimer, with

values of 2.638 Å, 2.619 Å, and 2.454 Å for B3PW91, B3LYP, and PBE0, respectively. At the B3LYP and PBE0 levels of theory, the chemisorbed copper dimers have smaller binding energies (121.2 and 140.0 kcal mol^{-1}, respectively) than two chemisorbed copper atoms (130.8 and 151.1 kcal mol^{-1}). In contrast, B3PW91 predicts the chemisorbed copper dimer to have a larger binding energy (148.7 kcal mol^{-1}) than separated chemisorbed copper atoms (134.6 kcal mol^{-1}.) This is a reflection of the fact that the Cu_2 dimer bond energies (42-43 kcal mol^{-1}) are only slightly smaller than the Al-Cu dimer bond energies (48-49 kcal mol^{-1}), as seen in Table 1. In other words, the energetic tradeoff between Cu-Cu binding vs. Al-Cu binding is more subtle than in the case of Au-Au vs. Al-Au discussed previously.

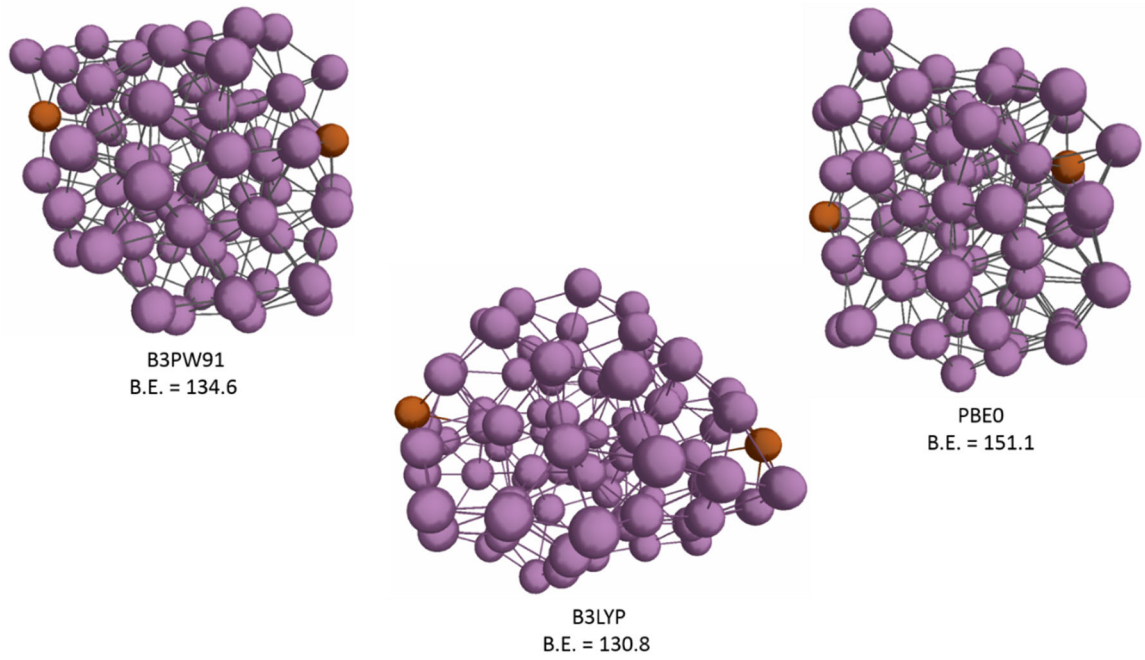

Figure 5. $Al_{80}{\cdot}Cu_2$ optimized structures with copper atoms on opposite side of the Al_{80} cluster. Binding energies are in kcal mol^{-1}.

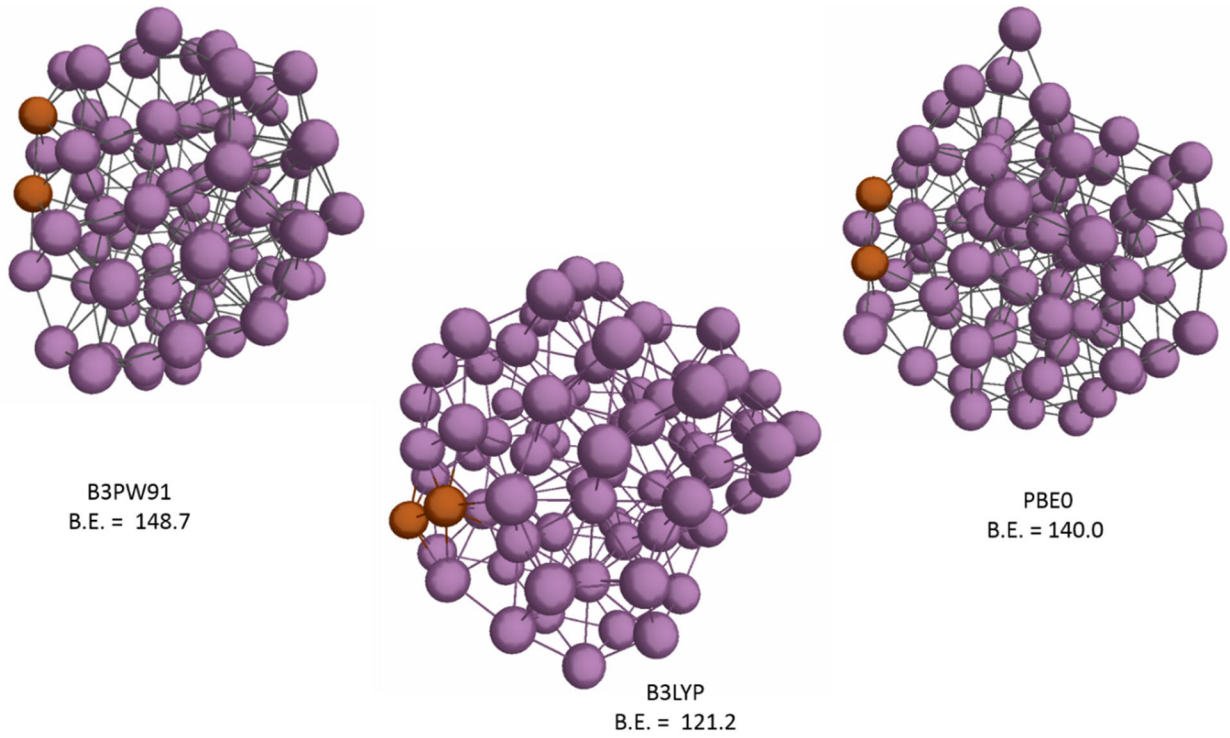

Figure 6. $Al_{80}{\cdot}Cu_2$ optimized structures with adjacent copper atoms on the cluster surface. Binding energies are in kcal mol^{-1}.

Analogous computations are also done for the Al/Si system, which is found to have similar characteristics to the previous systems. For instance, Si appears to bind strongly to the surface of the Al_{80} cluster. As can be seen in Figure 7, the Si atoms form multiple bonds to the surface, with binding energies ranging from 176.9 to 191.6 kcal mol^{-1}. Binding energies of the Si_2 dimer are slightly less than those of the separated atoms, ranging from 168.2 to 189.1 kcal mol^{-1}, as shown in Figure 8.

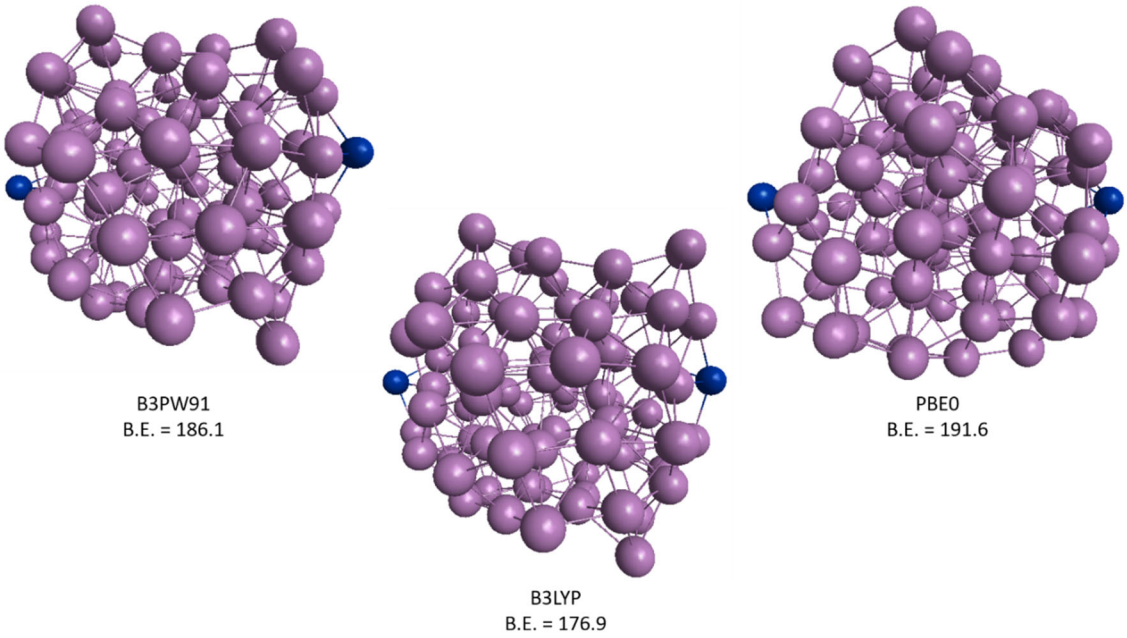

Figure 7. $Al_{80}{\cdot}Si_2$ optimized structures with silicon atoms on opposite side of the Al_{80} cluster. Binding energies are in kcal mol^{-1}.

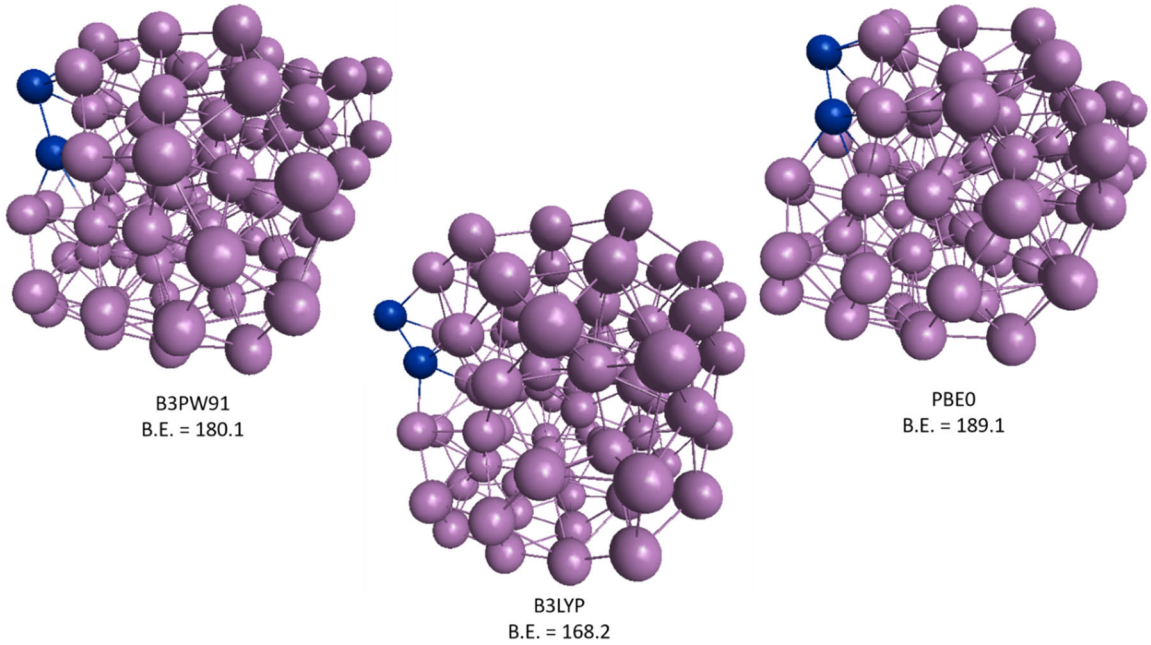

Figure 8. $Al_{80}{\cdot}Si_2$ optimized structures with adjacent silicon atoms on the cluster surface. Binding energies are in kcal mol^{-1}.

In investigating the ability for gold, copper, and silicon to have the fundamental chemistry available to coat an aluminum nanocluster to create a core-shell nanocluster, the calculations discussed above show clear evidence that this should be possible. All shell species chemisorb to the surface of the Al_{80} cluster with large binding energies ranging from 132.5-168.9 kcal mol^{-1} for two gold atoms, 121.2-151.1 kcal mol^{-1} for two copper atoms and 168.2- 191.6 kcal mol^{-1} for

two silicon atoms. The clusters in which the two atoms are located on opposite sides of the cluster tend to have larger binding energies than those in which they are next to each other, although this trend is less clear cut in the case of copper. In the cases of gold and copper, this observation is consistent with the fact that the shell atoms generally form stronger diatomic bonds with aluminum than with another gold or copper atom, as exhibited in the dimer calculations in Table 1. In contrast, the binding energies of silicon atoms on the Al_{80} cluster surface are slightly stronger than Si_2 dimers, despite the larger diatomic bond energy of Si-Si vs. Si-Al (60 and 27 kcal mol^{-1}, respectively, at the coupled cluster level). Of course, several additional factors also affect the relative stabilities of atomic vs. diatomic shell species on the cluster surface, such as local surface reconstruction, changes in atomic vs. diatomic vs. nanocluster electronic spin states, etc., which are not examined in detail here.

Possibility of Inversion

As previously mentioned above, in collaboration with colleagues at Eglin AFB, these clusters are synthesized via HDMD. During these He droplet experiments described above, introducing atomistic Al in the first pickup cell, forming Al nanoclusters and in a second pick up cell, another species is introduced such as atomistic gold, creating a passivating shell around the Al cluster. However, these experiments have also yielded no aluminum clusters, but oddly shaped Au rod-shaped clusters[37]. Previous work has shown that an inversion process may take place, as has been seen in the magnesium/copper system[38, 39]. It is suggested that due to the weak magnesium binding relative to that of copper, regardless of the order that the species are added, copper will always be found at the core. A generalization of this effect predicts that if the shell species has suitably stronger bonding relative to the core species, the shell layer can force its way into the core, leading to core-shell inversion. It is possible that this inversion process is occurring with the Al/Au clusters, with subsequent etching of the surface aluminum on the inverted nanoclusters, leaving only gold clusters behind. As such, the energetics involved in the possible inversion for both gold atoms into and Al cluster as well as Al atoms into a gold cluster are investigated. All optimizations were performed using the B3PW91 density functional with the SBKJC effective core potential and valence-only basis set, augmented with additional d and diffuse s+p functions on aluminum.

Fully optimized 30-atom clusters of aluminum and gold are obtained first and are seen in Figure 9. These clusters are used in the initial computations of two surface atoms located on opposite sides of the cluster. Initial structures of these systems are obtained systematically by first determining the center of mass of the 30-atom cluster and then placing the two additional surface atoms at a distance of 7 Å from the center on opposite sides of the 30-atom "parent" cluster. In order to get a more thorough picture of the energetics involved in the forced penetration of surface atoms into these clusters, three sets of computations are done in which the outer atoms are initially placed on the x-, y- and z-axis, as seen in Figure 10.

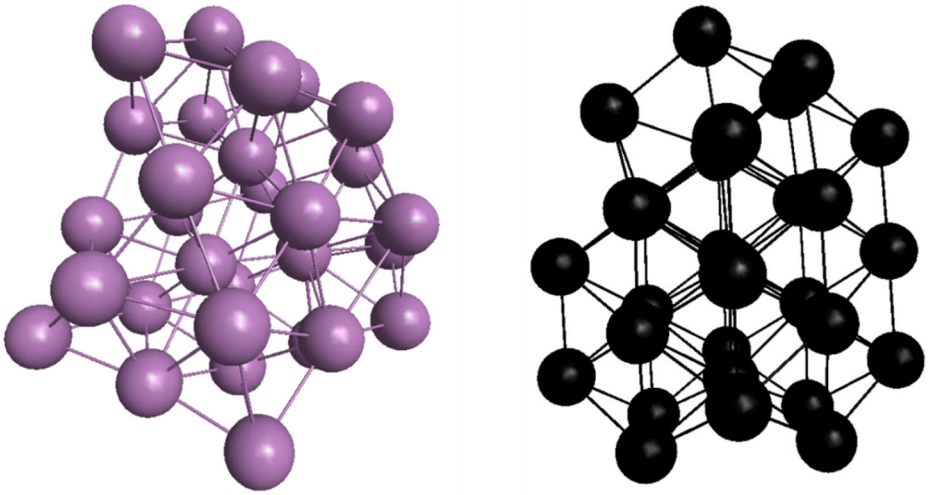

Figure 9. Structures of the Al_{30} and Au_{30} clusters, optimized at the B3PW91/SBKJC level of theory.

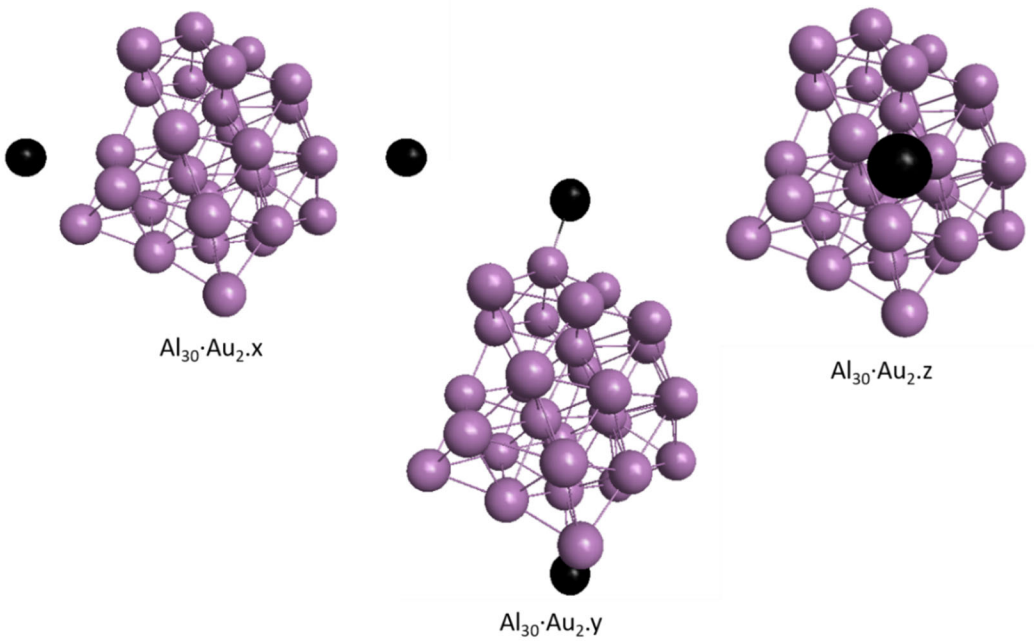

Figure 10. Initial structures used for full optimization calculations to find minima of surface absorbed structures.

These computations begin with full optimizations with no imposed constraints to obtain surface absorbed minima of all clusters. Once these local minima are located, a series of constrained optimizations are run in which the distance between the two outer atoms is restricted. In this series, the distance between the two surface atoms is reduced in steps of 0.25 Å in order to determine the potential energy surface (PES) of these atoms penetrating the cluster.

Al_{30}·Au_2

The first system investigated is the penetration of two gold atoms into the interior of an Al_{30} cluster. As can be seen in Figure 11, the initial unconstrained optimization of the cluster with the 2 gold atoms situated on the x-axis sit on the surface of the Al cluster at an Au-Au distance of 9.47 Å. As the gold atoms are forced into the cluster interior, the energy changes very little for nearly 3 Å along the PES, with two minor energy undulations as the gold atom on the left side perturbs the cluster and subsequent surface relaxation occurs. It is important to note that the cluster energies for R(Au-Au) between 6.5 and 9.0 Å are more stable than the initial local minimum with the Au atoms on the surface.

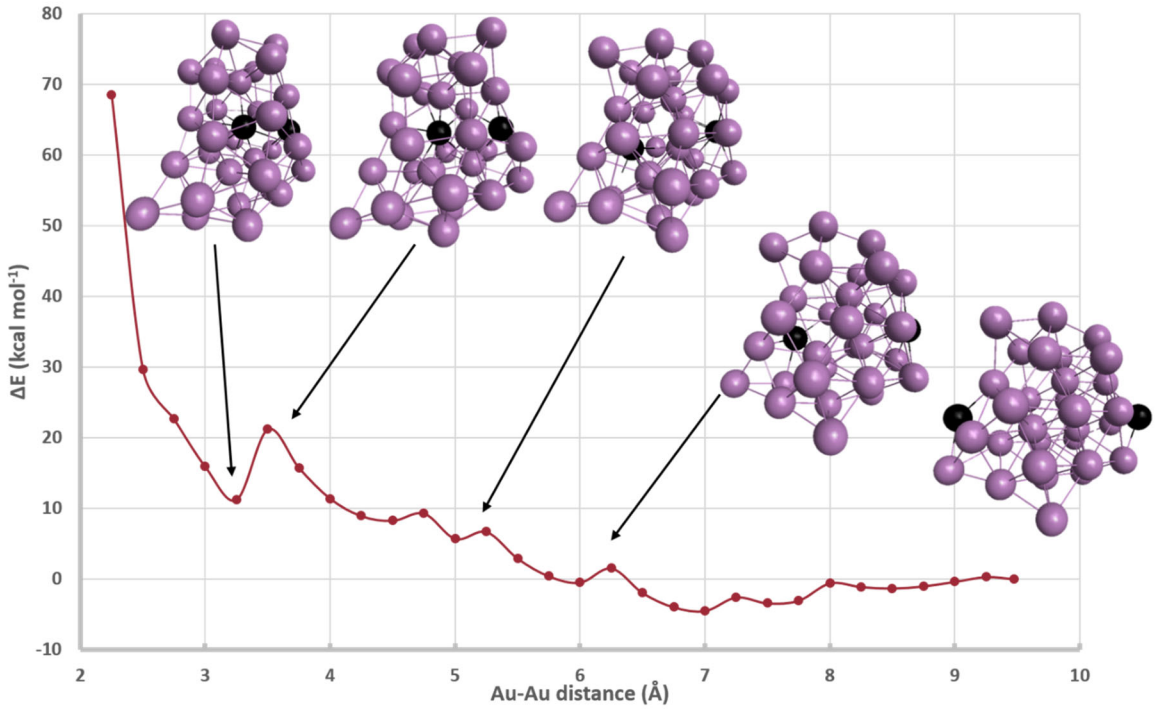

Figure 11. PES of 2 Au atoms situated along the x-axis being forced into an Al_{30} cluster.

As the Au-Au constrained distance continues to decrease from 6.50 Å, similar undulations are observed, but with a noticeable trend of increasing ΔE as a single gold atom fully penetrates the first shell of the cluster at an Au-Au distance of 4.50 Å, with an energy of 8.3 kcal mol^{-1}. The additional increase in ΔE from R(Au-Au)=4.50 to 3.50 Å is due to the same gold atom penetrating into the core of the aluminum cluster, reaching a maximum ΔE of 21.2 kcal mol^{-1} at an Au-Au distance of 3.50 Å. The drop in ΔE at an Au-Au distance of 3.25 Å is due to a significant rearrangement of the Al_{30} cluster, as seen in Figure 11. As the Au-Au distance continues to decrease, the energy sharply increases due to the repulsion of the Au atoms. As shown in Table 1, the computed equilibrium distance of the isolated Au dimer is ~2.55 Å, so Au-Au distances less than this are anticipated to be repulsive.

Figure 12, which shows only the two Au atoms and the three interior Al atoms present in the Au-Al_{30}-Au cluster at an Au-Au separation of 2.50 Å, highlights that one gold atom has penetrated the 3-atom Al "core", while the other Au atom resides on the surface. Figure 9 also shows the relative energies of the two fully optimized clusters starting from the constrained structures at Au-Au distances of 2.50 and 3.25 Å. Although the Au-Au distances slightly increase upon release of the constraint, the interior gold atom remains inside the cluster rather than migrating to the surface. This suggests that once a gold atom has penetrated the surface of the Al cluster, it is likely to remain in a metastable interior location rather than re-emerge onto the cluster surface.

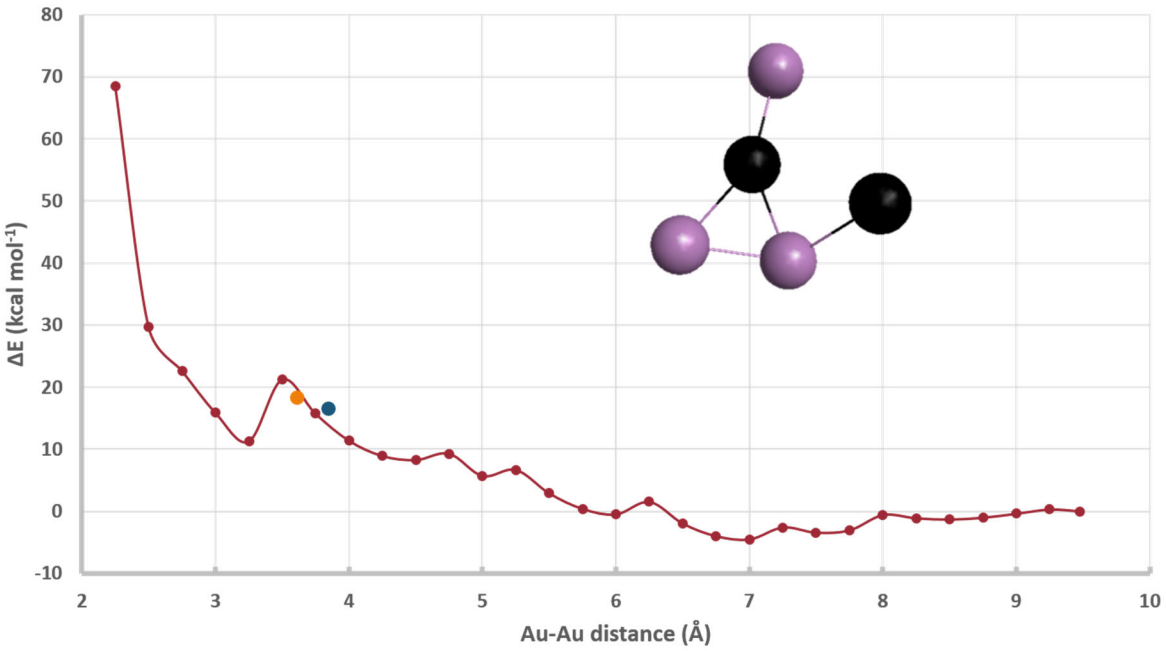

Figure 12. PES from Figure 11, showing only the structure of the 3-atom Al cluster "core" with the 2 Au atoms at R=2.50 Å. Full optimization at R=2.50 Å (Orange) and 3.50 Å (Blue).

As seen in Figure 13, the calculations with the gold atoms situated on the y axis are qualitatively similar to those on the x-axis (Figure 11). The initial structure has the gold atoms at a distance of 8.88 Å apart. There is initially a slight decrease in the ΔE followed by several undulations resulting from a single gold atom penetrating into the first layer of the Al cluster. However, the increase in ΔE as the Au-Au distance decreases to 2.50 Å is relatively uniform and less steep than in the approach along the x-axis. This is because the interior Au atom does not disrupt the 3-atom Al "core", but instead skirts around the edge as illustrated in Figure 14. Even so, while the core is not disturbed, it does appear that the energetics are similar to that of the x-axis calculations in that at R(Au-Au)=3.00 the ΔE is 18.42 kcal mol^{-1} on the y-axis and 15.9 kcal mol^{-1} on the x-axis. In both cases, the Au atom on the right side of the cluster stays on the surface while the other migrates into the cluster interior.

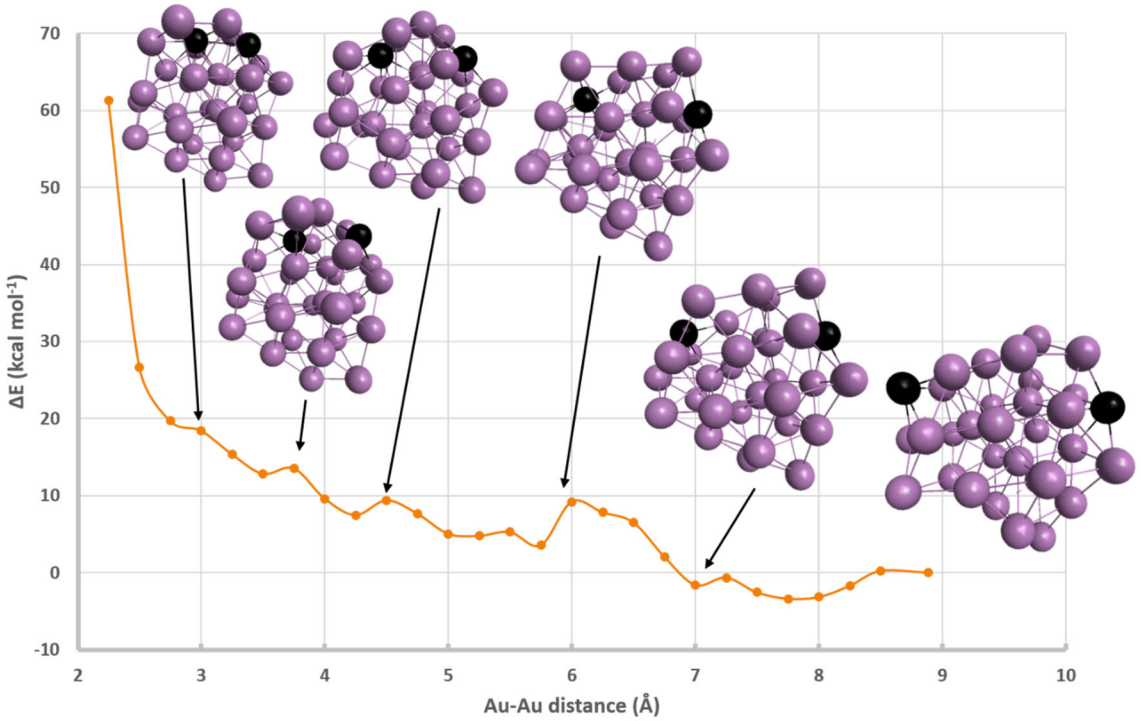

Figure 13. PES of 2 Au atoms situated along the y-axis being forced into an Al_{30} cluster.

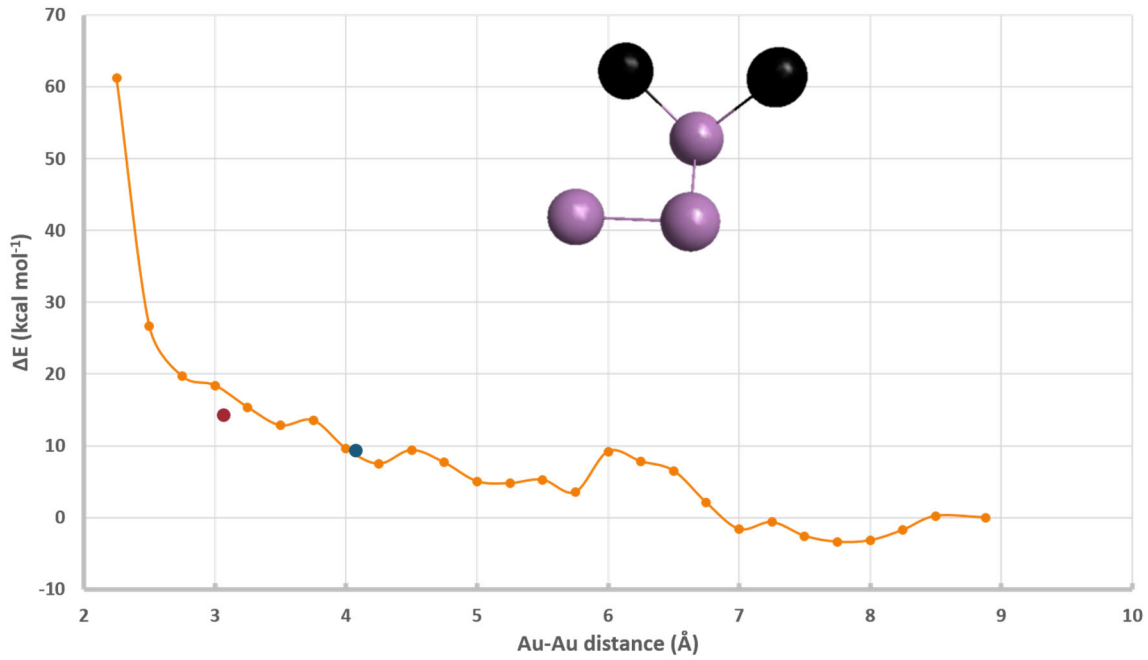

Figure 14. PES from Fig. 13 with structure of Al cluster "core" with the 2 Au atoms at R=2.50 Å. Full optimization at R=2.50 Å (Red) and 3.50 Å (Blue).

The calculations in which the Au atoms are put on the z-axis are unique in that this is the thinnest axis of the Al_{30} cluster, as can be seen in Figure 15. The initial structure has the Au atoms on the surface separated by a distance of only 7.70 Å. The relative energy varies modestly

as R(Au-Au) decreases from 7.70 to 6.50 Å. At R=6.25 Å, the Al_{30} cluster begins to "flatten" along the z-axis, with a decrease in relative energy to ~3 kcal mol^{-1}. As R continues to decrease to 5.75 Å, the energy rises as the Au atom on the left begins to migrate through the cluster surface, followed by a drop in energy at R=5.50 Å as the gold atom becomes more fully encapsulated by Al atoms. There is then a steady increase in the energy due to both Au atoms penetrating the cluster on each side simultaneously, up to R(Au-Au)=3.25 Å. Following a slight energy decrease at R=3.00, there is a significant increase due to the repulsion from the 2 Au atoms with the 3-atom Al core, up to R(Au-Au) = 2.50 Å. Further decreases in the Au-Au constraint lead to strong repulsive interactions, driving the total energy higher, similar to the energy profiles along the x-axis and y-axis at short R(Au-Au) distances, shown in Figures 11 and 13, respectively.

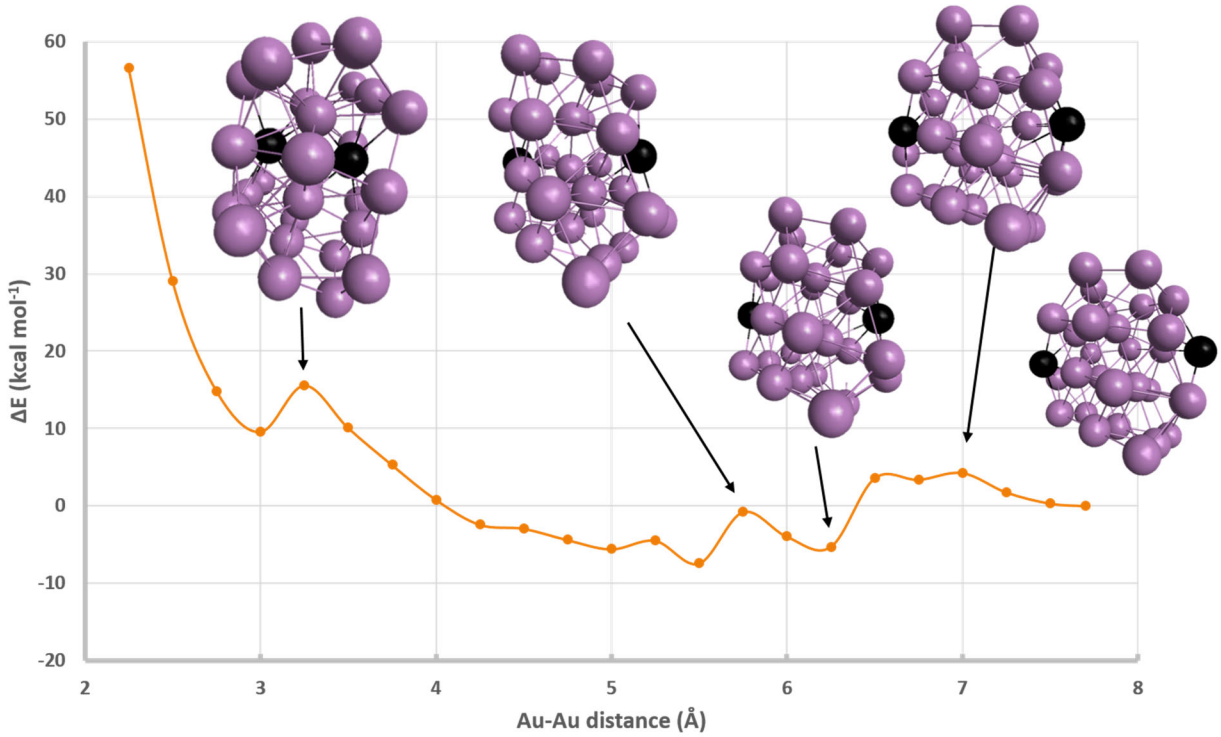

Figure 15. PES of 2 Au atoms situated along the z-axis being forced into an Al_{30} cluster.

At close Au-Au distances along the z-axis, the Au atoms do not penetrate the core of the Al cluster, but reside on either side of it at an Au-Au distance of 3.0 Å as seen in Figure 16. Also shown in Figure 16 are the final relative energies and Au-Au separations in fully optimized structures which were initiated at R(Au-Au)=2.5 and 5.0 Å. In contrast to the corresponding

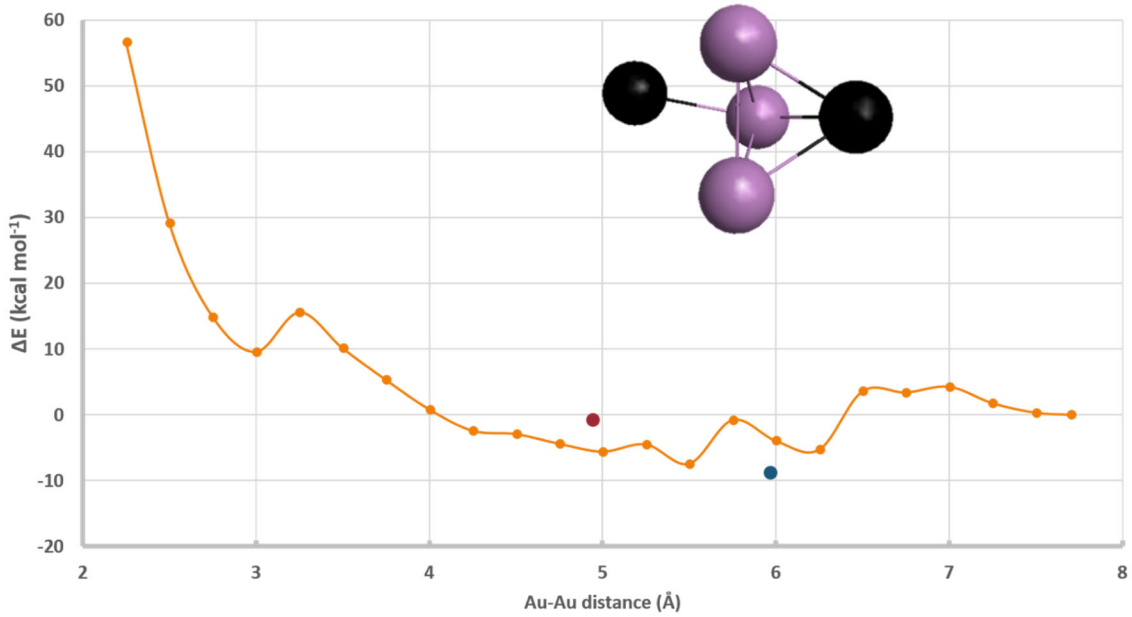

Figure 16. PES from Fig. 12, showing only the 3-atom Al cluster "core" and the two Au atoms at R=2.50 Å. Full optimization at R=2.50 Å (Red) and 5.00 Å (Blue)

fully relaxed clusters obtained from the constrained x-axis and y-axis potential energy curves (Figures 11 and 13, respectively,) the Au-Au distance lengthens significantly upon release of the constraint. For example, starting from the constrained structure at R=2.5 Å, cluster reoptimization in the absence of the constraint increases the Au-Au distance to R≈5 Å. Similarly, the R=5.00 constrained structure fully relaxes to R≈6 Å.

Despite the detailed differences between the three constrained pathways, the overall energy profiles of the three pathways are qualitatively similar, as shown in the composite PES plot in Figure 17, which includes the average of the three individual potential energy curves.

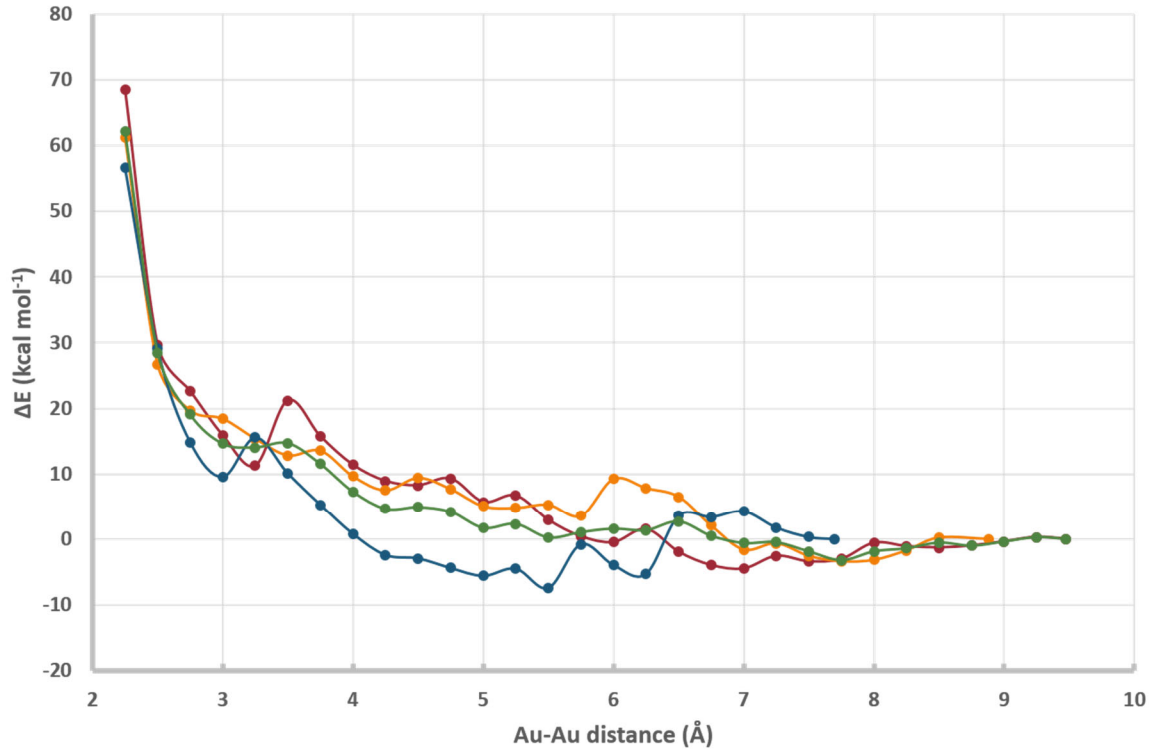

Figure 17. Composite plot of the PESs of 2 Au atoms, situated along the x- (Red), y- (Orange), and z-axis (Blue), being forced into an Al_{30} cluster. Also shown is the average (Green) of the x-, y-, and z-axis curves.

$Au_{30}{\cdot}Al_2$

Initial calculations for inversion as discussed above were also done for the $Au_{30}{\cdot}Al_2$ system. Interestingly, the initial unconstrained optimizations for $Au_{30}{\cdot}Al_2$ result in one fully embedded and one partially embedded Al atom, rather than both Al atoms remaining on the Au_{30} cluster surface. This is shown in Figure 18, which includes a trace of the total electronic energy during the course of the full optimization of $Au_{30}{\cdot}Al_2$ in which the Al atoms are originally placed along the x-axis. There is noticeable change in the structure of the Au cluster, which transitions from an ordered to a more amorphous cluster structure. Since the optimization does not result in a local minima with the Al atoms on the surface, but with the Al atoms embedded in the Au cluster, this suggests that Al atoms can migrate into the interior of Au clusters with little or no energy barrier. Therefore, no additional studies of Al migration into Au_{30} were performed. This result, along with the $Al_{30}{\cdot}Au_2$ work mentioned above, is in good qualitative agreement with experimental studies on the passivation of Al nanoparticles with gold, in that gold performed the worst among Au, Ni, Pd, and Ag in terms of preventing oxidation of active Al[40, 41].

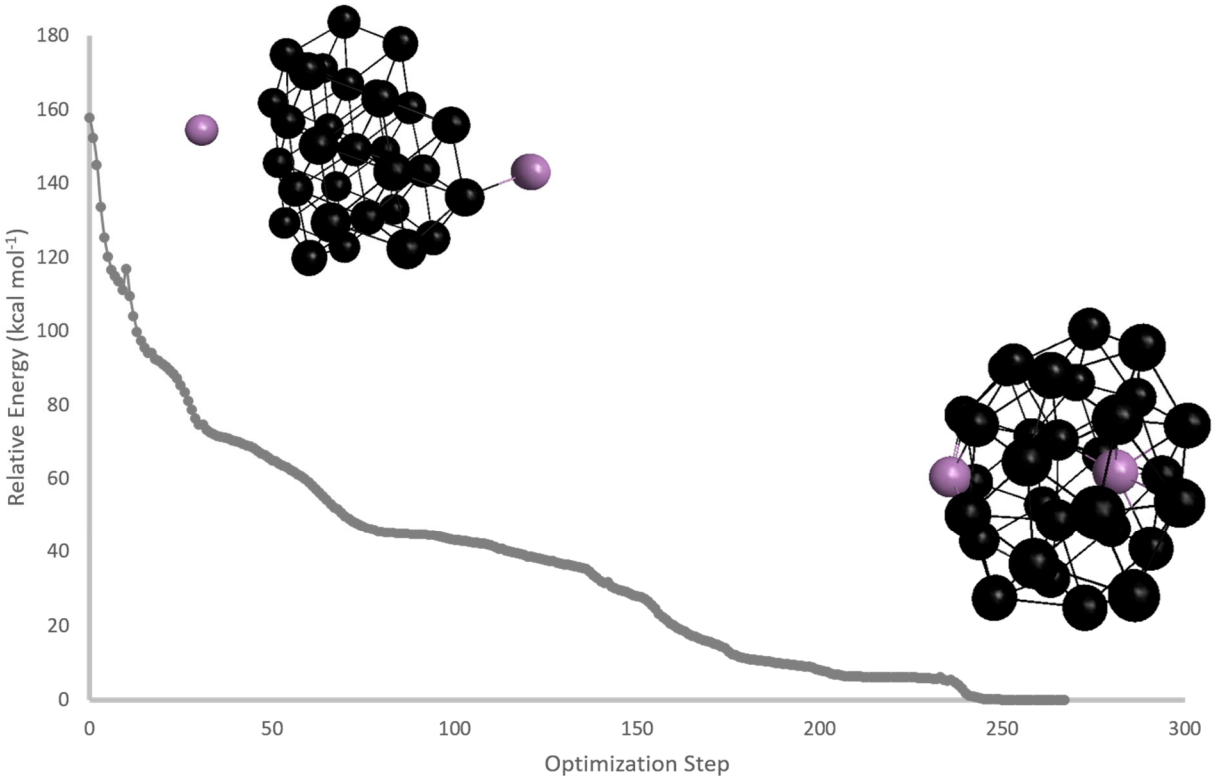

Figure 18. Trace of B3PW91/SBKJC electronic energies during the course of an optimization of two Al atoms interacting with an Au_{30} cluster, with resulting optimized structure having one Al atom in the surface of the cluster. Energies are in kcal mol^{-1}, relative to the fully optimized $Au_{30}{\cdot}Al_2$ cluster.

$Al_{30}{\cdot}Si_2$

Similar calculations to those above for the Al/Au system are also done for the Al/Si system, beginning with $Al_{30}{\cdot}Si_2$. With the silicon atoms placed on the x-axis, the initial structure has the silicon atoms on the surface of the cluster separated by a distance of 11.18 Å, as seen in Figure 19A, with a binding energy of 178.0 kcal mol^{-1}. The ΔE increases rapidly from the outset due to the Si perturbing the structure of the Al cluster (Fig. 19B) as the Si atoms are forced together, generating a local ΔE maxima of 8.28 kcal mol^{-1} occurring at an Si-Si distance of 10.25 Å. This is followed by a drop in energy as the Al_{30} cluster undergoes rearrangement (Fig. 19C) in response to the constrained Si atoms. It is not until the Si atoms are 6.75 Å apart (Fig. 19D) that the Si atom on the right begins to penetrate the Al_{30} cluster, resulting in an increase in ΔE to 12.9 kcal mol^{-1}. At R=6.5 Å, the Al cluster undergoes modest rearrangement to a slightly more stable structure. As R continues to decrease to 5.25 Å, the energy sharply rises to a local maximum of 23.1 kcal mol^{-1}, with the Si atom on the right completely encapsulated in the Al cluster interior (Fig. 19E). As R decreases to 3.00 Å, the Si atom on the left begins to penetrate the cluster as well (Fig. 19F) with a ΔE of 22.6 kcal mol^{-1}. This is followed by another rearrangement of the Al cluster to accommodate the Si atoms (Fig. 19G) which is seen in a drop of ΔE to 13.0 kcal mol^{-1} at R=2.75 Å. At this point, the Si atoms have disrupted the three

interior "core" atoms of the Al cluster (Figure 19H,) similar to what was observed in Al_{30}·Au_2 (Fig. 12E.)

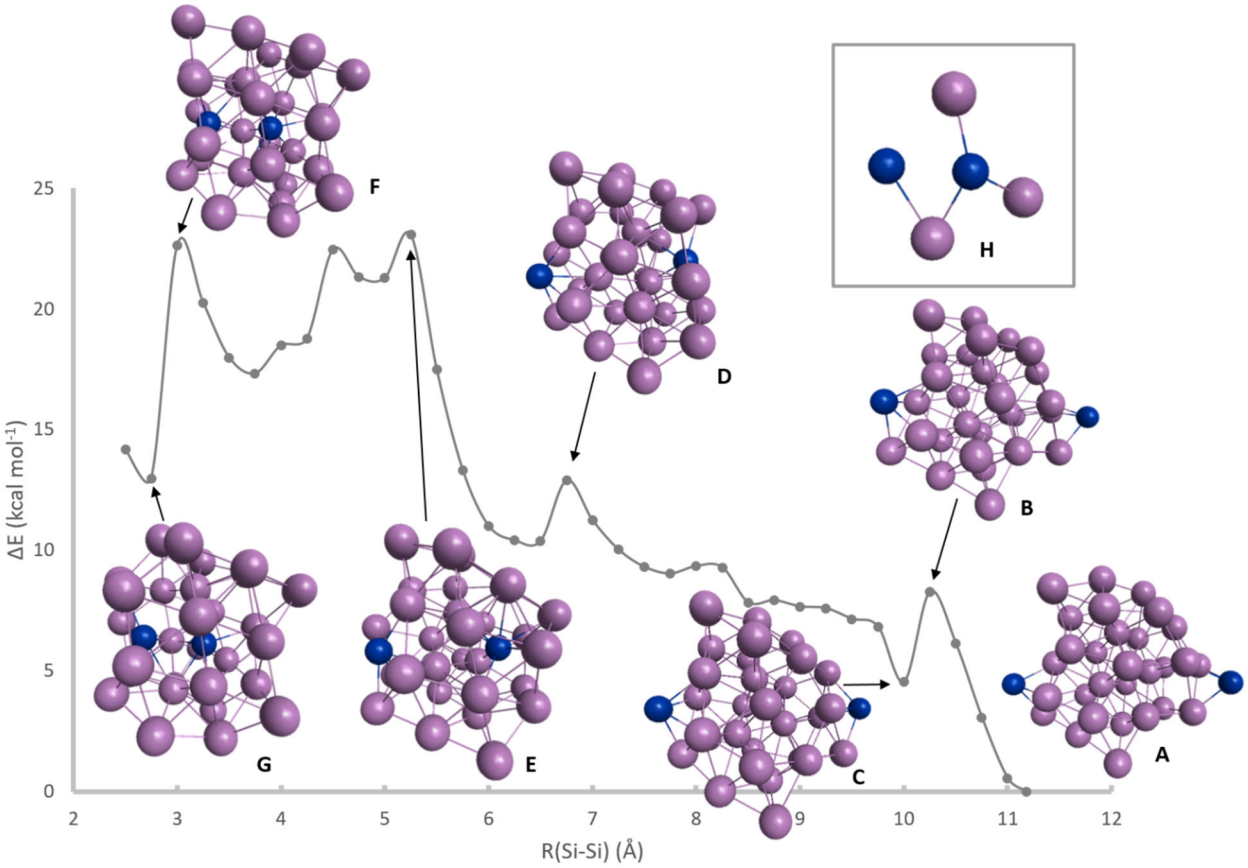

Figure 19. B3PW91/SBKJC potential energy surface scan of the migration of two Si atoms situated on the x-axis into an Al_{30} cluster as a function of Si-Si distance. Inset (H): structure of 3-atom Al "core" with the 2 Si atoms at R=2.75 Å.

The system in which the Si atoms are situated on the y-axis, as illustrated in Figure 20, shows the initial structure (A) with the Si atoms separated by 11.10 Å having a binding energy of 189.4 kcal mol^{-1}. From this point the relative energy increases significantly due to Al cluster deformation in which both Si atoms stay on the surface (Fig. 20B), generating a local ΔE maxima of 22.6 kcal mol^{-1} at a Si-Si distance of 9.5 Å. This is followed by a rearrangement in the Al cluster (Fig. 20C), lowering the ΔE to 18.7 kcal mol^{-1} at R(Si-Si)=9.0 Å. This undulation in ΔE happens several times as illustrated in Fig. 20D&E in which the Si atom on the left side of the cluster begins to penetrate Al_{30}, followed by a rearrangement of the cluster to return the Si atom to the surface, effectively resulting in the Si atom sliding along the surface of the Al_{30} cluster. Similar behavior of the Si atom on the right side occurs as R continues to decrease to 4.25 Å (Fig. 20F&G.) The highest local ΔE maxima of 40.8 kcal mol^{-1} occurs at R(Si-Si)=2.75 Å, at which point the Si atoms begin bonding together on the cluster surface (Fig. 20H&I.)

Since both Si atoms remain on the surface, the three-atom interior Al cluster "core" remains undisturbed, as shown in Fig. 20J.

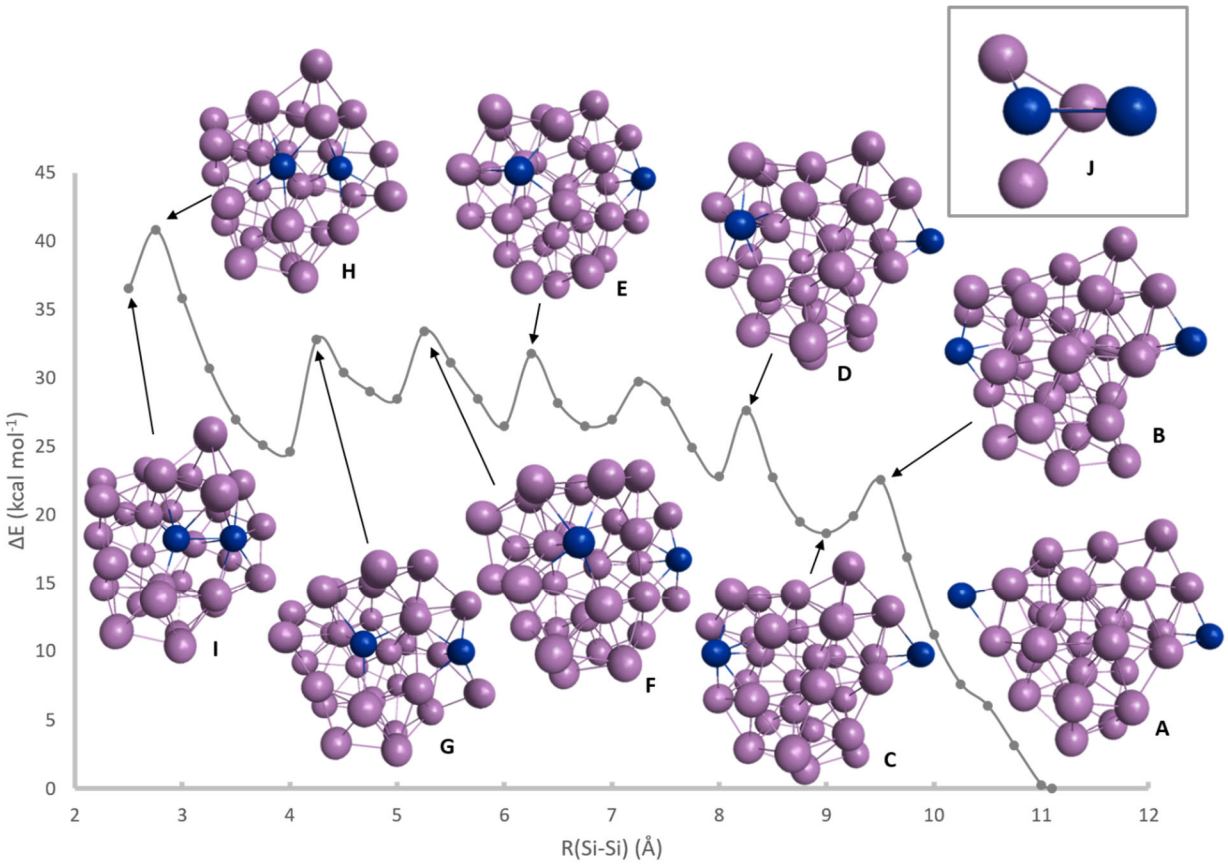

Figure 20. B3PW91/SBKJC potential energy surface scan of the migration of two Si atoms situated on the y-axis into an Al_{30} cluster as a function of Si-Si distance. Inset (J): structure of 3-atom Al "core" with the 2 Si atoms at R=2.50 Å.

A remarkably different picture emerges when the Si atoms are initially placed along the z-axis, as shown in Figure 21. The fully optimized initial structure has the two Si atoms on the surface separated by 9.9 Å (Fig. 21A) with a binding energy of 170.4 kcal mol^{-1}. Initially, the relative energy rises to 5.9 kcal mol^{-1} at a Si-Si distance of 9.0 Å (Fig. 21B). However, at R(Si-Si)=8.75 Å, the energy decreases to -6.7 kcal mol^{-1}, becoming more stable than the initial, fully optimized cluster at R(Si-Si)=9.9 Å. As the Si-Si distance continues to decrease, the Si atom on the right side of the cluster begins penetrating the cluster surface (Fig. 17C.) At R(Si-Si)=6.5 Å, the Si on the right has become fully embedded (Fig. 21D.) This is followed by another rearrangement of the underlying Al_{30} cluster, resulting again in a configuration which is [~6 kcal mol^{-1}] more stable than the original cluster at R(Si-Si)=9.9 Å. Next, the Si atom on the left begins penetrating the surface of the cluster, rising in energy to 13.2 kcal mol^{-1} (Fig. 21E) at R(Si-Si)=5.25 Å. The Al cluster then undergoes another large rearrangement, followed by the penetration of the Si atom on the left into the cluster (Fig. 21F,) resulting in the global maximum ΔE of 23.3 kcal mol^{-1} at R(Si-Si)=2.75 Å. This is followed by the formation of a Si-Si bond as

seen in Fig. 21G. It is clear that the original Al cluster undergoes a great amount of rearrangement from the penetration of the two Si atoms, as can clearly be seen in Fig. 21H, which depicts the disruption of the three-atom Al "core" by the embedded Si atoms. Because of the massive structural rearrangements, Al_{30} optimization calculations were run beginning at the rearranged geometries at R(Si-Si)=8.75, 6.25 and 4.75 Å, with the Si atoms removed. For the reoptimization of the underlying Al_{30} cluster initiated at R(Si-Si)=4.75, the resulting relaxed Al_{30} cluster structure was found to be 2.6 kcal mol^{-1} more stable than the initial Al_{30} cluster.

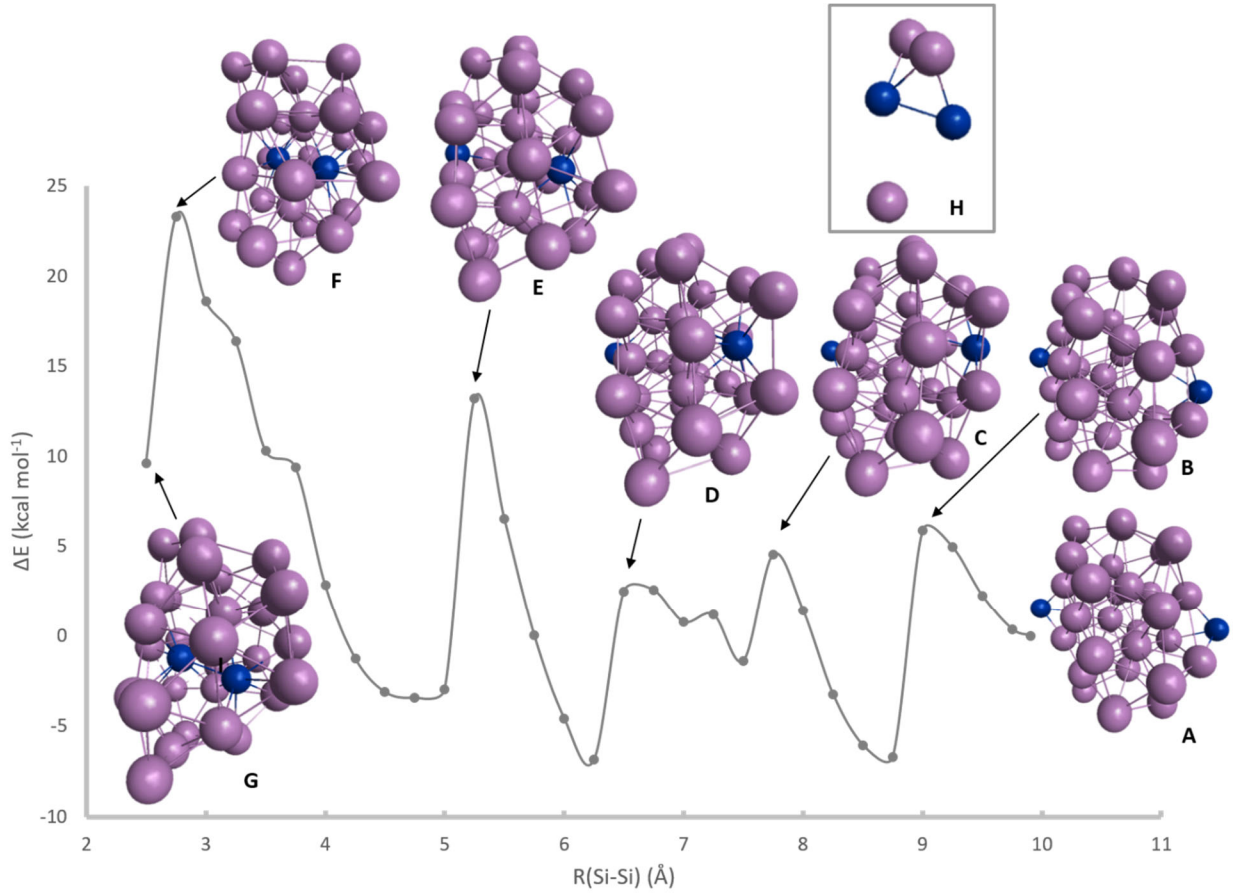

Figure 21. B3PW91/SBKJC potential energy surface scan of the migration of two Si atoms situated on the z-axis into an Al_{30} cluster as a function of Si-Si distance. Inset (H): structure of 3-atom Al "core" with the 2 Si atoms at R=2.50 Å.

The contrast in behavior of these three energy scans is highlighted in the composite PES plot shown in Figure 22. While all three energy surfaces show an increase in ΔE at the outset as the surface Si atoms are initially forced together, the energy profiles diverge as R(Si-Si) continues to decrease. The least energetically favorable approach, along the y-axis, corresponds to the silicon atoms sliding along the surface of the cluster, culminating in formation of a Si_2 dimer on the surface and traversing a maximum ΔE of 40.8 kcal mol^{-1}. The more energetically favorable approaches, along the x and z axes, result in the silicon atoms entering the interior of the Al_{30} cluster, with each encountering a maximum ΔE of 23 kcal mol^{-1}. Relative to the y-axis

scan, the approach along the z-axis results in more dramatic structural rearrangements, including relaxation to intermediate structures which are more stable than the initial local minimum.

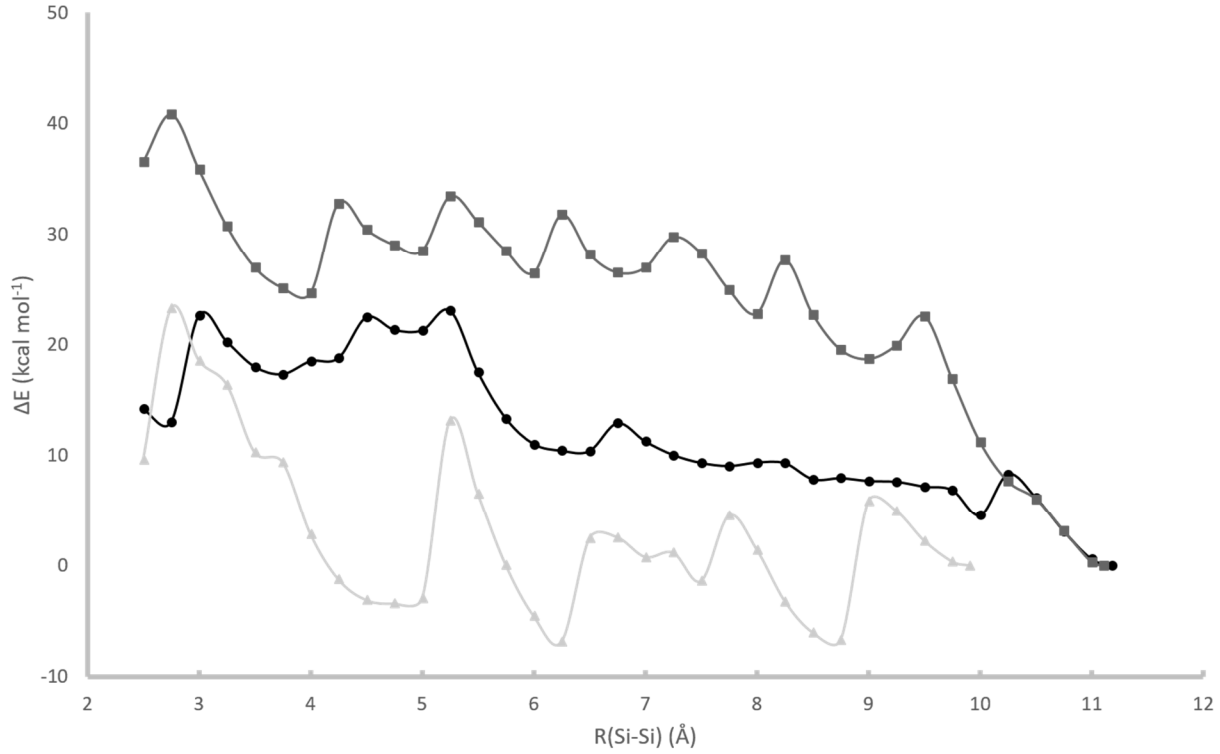

Figure 22. B3PW91/SBKJC potential energy surface scans of the migration of two Si atoms situated on the x- (●), y- (■), z-axis (▲) into an Al_{30} cluster as a function of Si-Si distance. Energies are in kcal mol^{-1}, relative to each initial fully optimized $Al_{30}{\cdot}Si_2$ cluster.

$Si_{30}{\cdot}Al_2$

Analogous calculations are also done for the inverse $Si_{30}{\cdot}Al_2$ system, with 2 Al atoms initially on the surface of and penetrating into a Si_{30} cluster. With the aluminum atoms placed on the x-axis, the initial structure has the Al atoms on the surface of the cluster separated by a distance of 9.64 Å, as seen in Figure 23A, with a binding energy of 92.2 kcal mol^{-1}. Initially, the ΔE increases only slightly to 1.3 kcal mol^{-1} (Fig. 23B.) This is followed by a decrease in energy as the Si_{30} cluster rearranges and becomes more stable than the initial fully optimized structure at R(Al-Al)=9.64 Å. It is not until the Al atoms are 5.50 Å apart (Fig. 23C) that an Al atom begins to penetrate the Si_{30} cluster, exhibited by the increase in ΔE to 5.13 kcal mol^{-1}. Next, there is a significant rearrangement and stabilization of the Si cluster at an Si-Si distance of 4.25 Å (Fig. 23D) as the Al atom on the left becomes fully encapsulated inside the Si_{30} cluster, resulting in a ΔE that is 46.7 kcal mol^{-1} below that of the initial cluster. As R(Si-Si) continues to decrease, there is some addition rearrangement and stabilization of the system (Fig. 23E) with a ΔE of -57.6 kcal mol^{-1}. It is clear from this PES that there is little barrier for Al penetration into a small

Si cluster and that the overall process of Al encapsulation is energetically favorable. However, it should be noted that the Si_{30} cluster does not have an inner "core" like the Al_{30} cluster, so this penetration is only into the outer layer of the Si cluster.

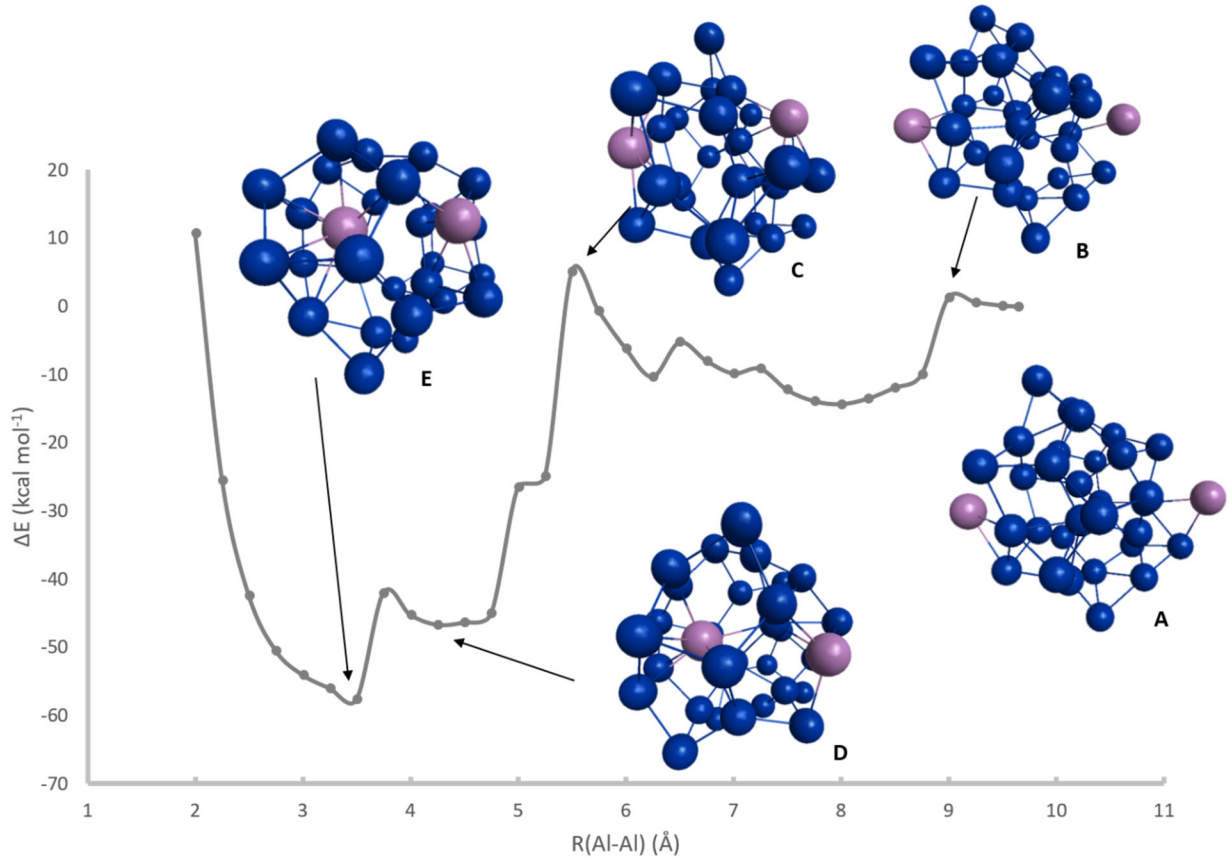

Figure 23. B3PW91/SBKJC potential energy surface scan of the migration of two Al atoms situated on the x-axis into a Si_{30} cluster as a function of Al-Al distance.

With the aluminum atoms placed on the y-axis, the Al atoms initially are 13.17 Å apart, as shown in Figure 24A, with a binding energy of 99.1 kcal mol^{-1}. The ΔE gradually increases to 3.3 kcal mol^{-1} as the Al-Al distance decreases to 10.50 Å (Fig. 24B), corresponding to the Al atom on the right moving along the cluster surface. After a modest rearrangement to a more stable structure at R(Al-Al)=9.5 Å, the relative energy gradually increases again as the Al atom on the right continues to move laterally across the Si_{30} surface until the Al atoms are 7.00 Å apart (Fig. 24C), with a corresponding increase in ΔE to 12.1 kcal mol^{-1}. This is followed by a significant rearrangement of the Si cluster, relaxing the energy of the system to 4.0 kcal mol^{-1} below that of the initial cluster, at a Al-Al distance of 5.75 Å (Fig. 24D). At this point, both Al atoms remain on the surface, with a single intervening Si atom. As the Al-Al distance continues to decrease, ΔE rises rapidly to 19.8 kcal mol^{-1} at an Al-Al distance of 3.75 Å (Fig. 24E), at which point the Si atom located between the Al atoms has been shunted to the side. This is followed by another major rearrangement to a structure (Fig. 24F) which is 8.3 kcal mol^{-1} more

stable than the original cluster, energetically driven in part by formation of the Al_2 dimer on the Si_{30} cluster surface.

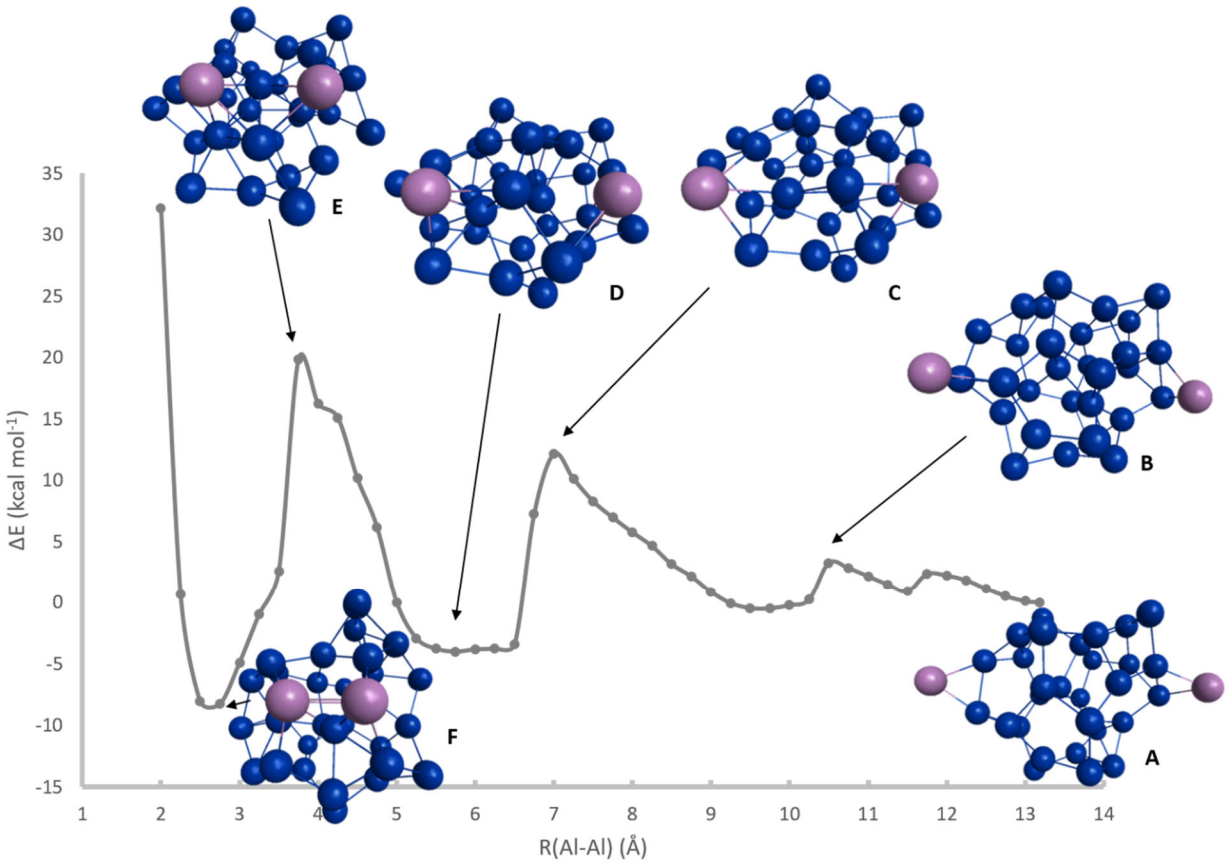

Figure 24. B3PW91/SBKJC potential energy surface scan of the migration of two Al atoms situated on the y-axis into a Si_{30} cluster as a function of Al-Al distance.

With the aluminum atoms placed on the z-axis, the initial structure has the Al atoms on the surface of the cluster separated by a distance of 10.60 Å, seen in Figure 25A, with a binding energy of 107.8 kcal mol^{-1}. The relative energy shows modest fluctuations as R(Al-Al) decreases to 8.0 Å, then increases to 15.0 kcal mol^{-1} at R=7.75 Å , due to the Al on the left beginning to penetrate the Si cluster surface (Fig. 25B). This is followed by a rearrangement of the cluster, with both atoms partly embedded into the cluster at R=4.75 Å (Fig. 25C) with a ΔE of 1.1 kcal mol^{-1}. Subsequently at R=4.50 Å, a significant rearrangement occurs, leaving both Al atoms embedded in the Si cluster, with an energy of -23.3 kcal mol^{-1} relative to the initial structure. As R(Al-Al) decreases to 3.25 Å, the energy rises to -2.2 kcal mol^{-1} (Fig. 25D), at which point both Al atoms have penetrated the Si cluster surface. At R=3.0 Å another major structural rearrangement takes place (Fig. 25E), resulting in the most stable point on this PES with a relative energy of -39.1 kcal mol^{-1}.

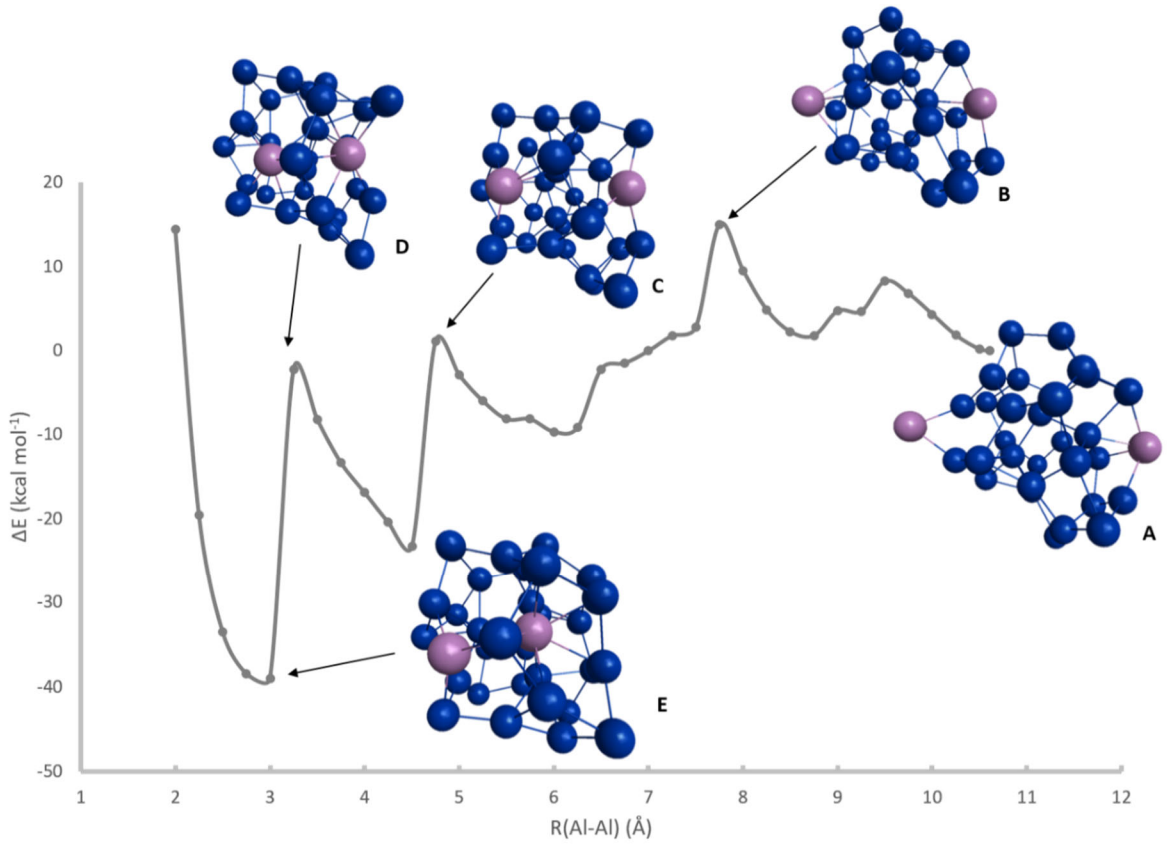

Figure 25. B3PW91/SBKJC potential energy surface scan of the migration of two Al atoms situated on the z-axis into a Si_{30} cluster as a function of Al-Al distance.

The Si_{30}·Al_2system exhibits 3 distinct energy profiles depending on the initial orientation of the Al atoms, as shown in Figure 26. With the Al atoms initially on the x-axis, there is a modest barrier for the Al to penetrate the cluster, with a maximum ΔE of 5.13 kcal mol^{-1} and the energetically most favorable structure (ΔE of -57.6 kcal mol^{-1}) having a single Al wholly encapsulated within the Si cluster and the other Al remaining on the surface. In sharp contrast, approach of the Al atoms along the y-axis results in formation of the Al dimer on the Si cluster surface with ΔE of -8.3 kcal mol^{-1}, with an intervening maximum ΔE of 19.8 kcal mol^{-1}. The z-axis PES is qualitatively similar to that of the x-axis, with the most stable structure (ΔE = -39.1 kcal mol^{-1}) corresponding to a single encapsulated Al atom and a maximum ΔE of +15.0 kcal mol^{-1}.

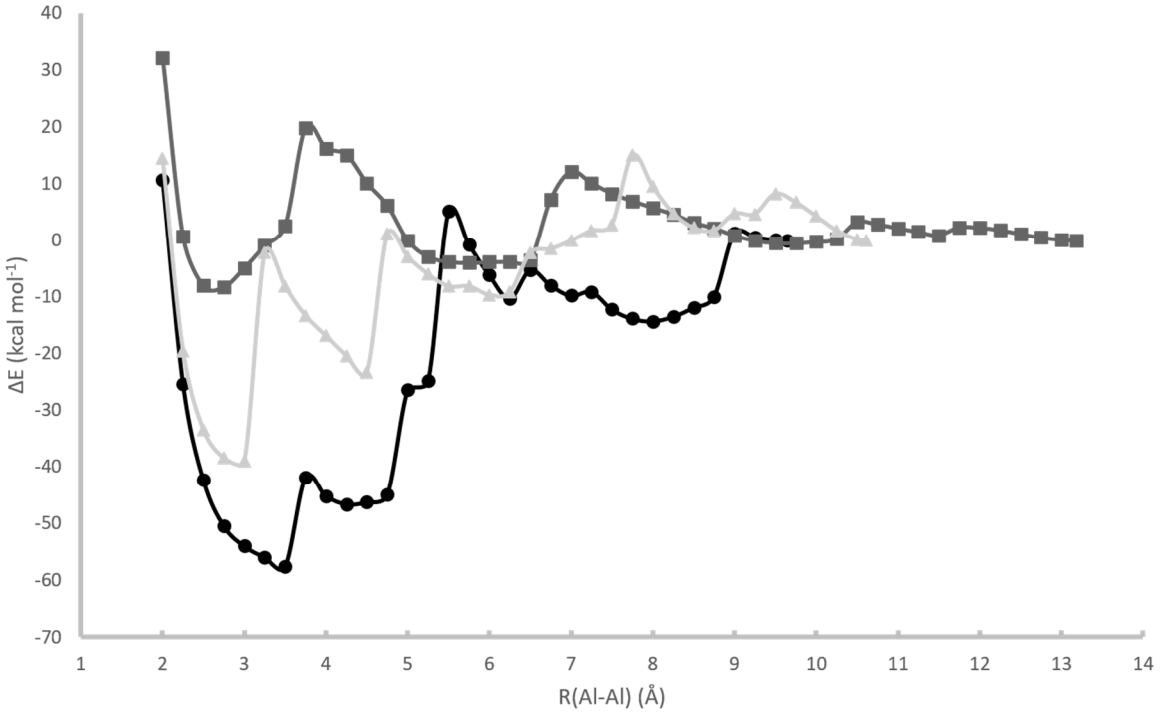

Figure 26. B3PW91/SBKJC potential energy surface scans of the migration of two Al atoms situated on the x- (●), y- (■), z-axis (▲) into a Si_{30} cluster as a function of Al-Al distance. Energies are in kcal mol^{-1}, relative to each initial fully optimized $Si_{30}{\cdot}Al_2$ cluster.

Al Cluster Oxidation

In conjunction with experimental studies on Al core-shell nanocluster formation conducted by collaborators at AFRL/RW (Eglin AFB), there is a critical need for a fundamental understanding of the core-shell nanocluster formation processes and the nature of the chemical and physical interactions at the core-shell interface. Nanoclusters are synthesized through the use of helium droplets which are formed via supersonic expansion and then travel through a pick-up cell containing gas-phase atomic Al, as previously discussed above. However, such experiments to synthesize pure Al nanoclusters have yielded no cluster formation. Electron ionization mass spectrometry confirms that Al is being picked up by the He droplets, but yielding no clusters upon deposition[37]. It is possible that these clusters undergo oxidative etching[42-44] when exposed to air upon deposition. As such, we investigate the energetics involved in the oxidative etching of Al clusters. The oxidative etching process is studied via the loss or "etching" of the simple aluminum oxide species Al_2O. Al oxidation has also been suggested by our collaborators at Eglin to be important factor in the inversion process mentioned above. All calculations are done utilizing using the B3LYP functional and the SBKJC effective core potential plus valence-only basis set, as mentioned previously.

The oxidative etching of Al clusters is studied from two different perspectives. First is the oxidative process of a single oxygen molecule with an Al_{30} cluster, whose potential energy surface (PES) is seen in Figure 27. It is important to note the spins states of all species, with the initial reactants of Al_{30} and O_2 being in their ground singlet and triplet state respectively.

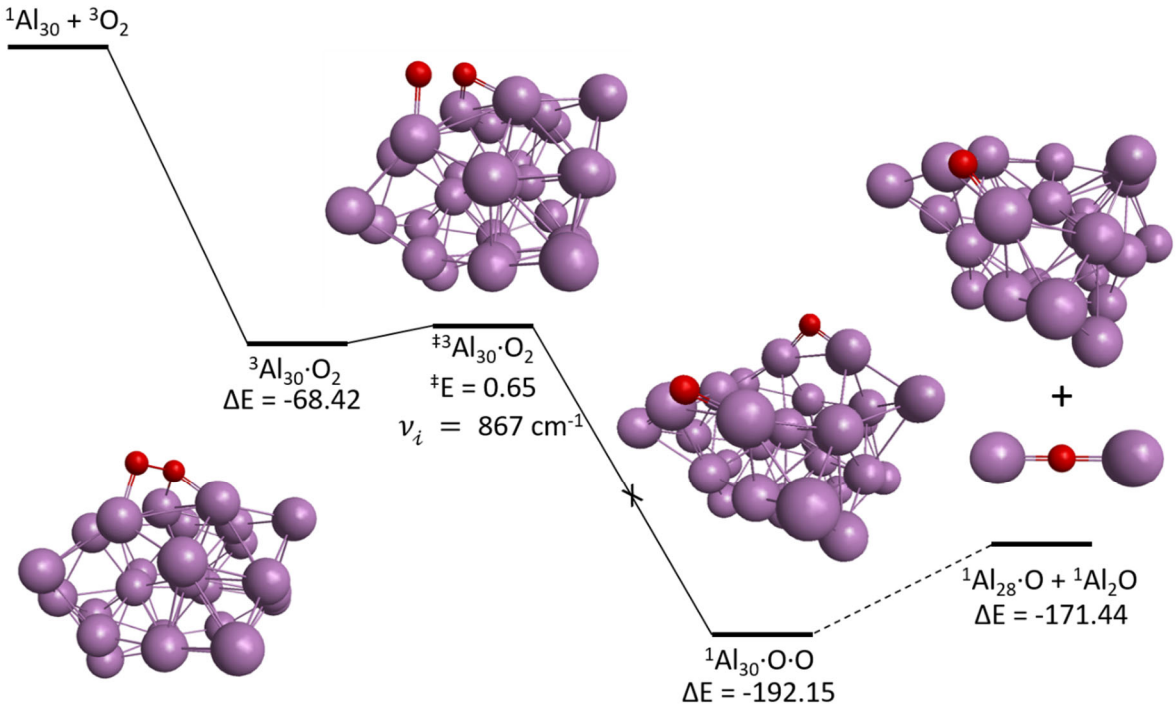

Figure 27. Potential Energy Surface of $^1Al_{30} + {}^3O_2$ calculated at the B3LYP/SBKJC level of theory. Energies are in kcal mol^{-1} and include zero point energy (ZPE) corrections, potential energy surface is not to scale.

An intermediate complex is formed on the triplet surface in which the O_2 molecule is absorbed on the surface of the Al_{30} cluster with one oxygen atom being associated with two surface Al atoms and the other oxygen atom associated with only one surface Al atom, yielding a binding energy of 68.42 kcal mol^{-1}. This goes through a transition state, also on the triplet surface in which the O-O bond breaks with an activation energy of 0.65 kcal mol^{-1} with respect to the intermediate complex and -67.77 kcal mol^{-1} with respect to the reactants. After this transition state, the PES crosses from the triplet surface to the singlet surface. This surface crossing can be seen in Figure 28, which shows the intrinsic reaction coordinate (IRC) for the transition state on the triplet surface, alongside single point energy computations at given geometries.

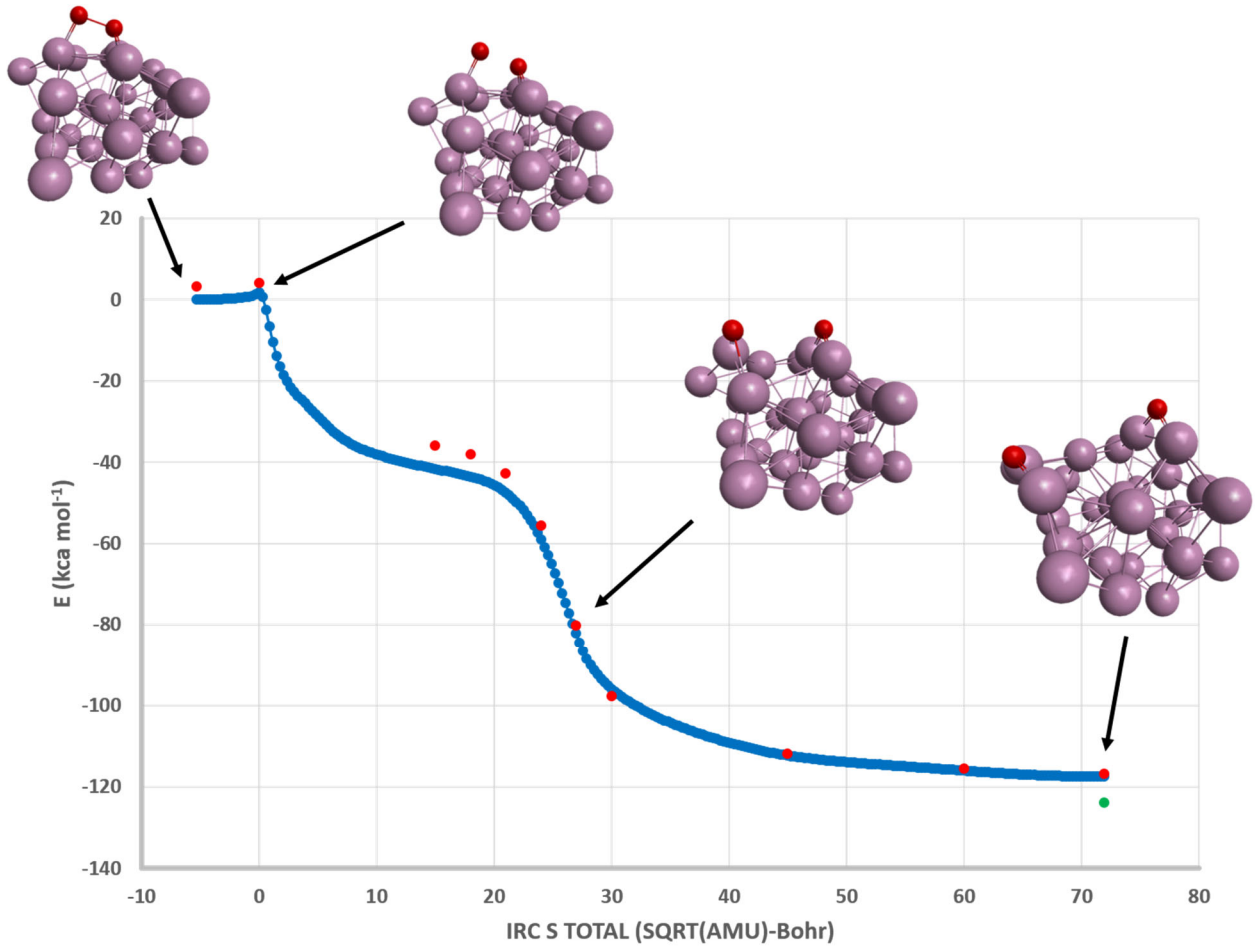

Figure 28. Triplet state intrinsic reaction coordinate (IRC) (blue) for the decomposition of O_2 on the surface of an Al_{30} Cluster. Singlet state single point energies at selected points on the triplet IRC are shown as red dots. The energy of the fully optimized singlet state, starting from the final point on the triplet IRC, is shown by the green dot.

The singlet-triplet surface crossing appears to occur at a point along the IRC where both oxygen atoms become fully bonded to the Al cluster surface, each being associated with two surface aluminum atoms. While the single point energies on the singlet surface are very similar to those on the triplet surface, a full optimization on singlet surface as seen on the final IRC point is clearly lower in energy. The post transition state intermediate minimum with two separated oxygen atoms lies -192.15 kcal mol^{-1} with respect to the reactants, as seen in Figure 27. The thermodynamic energetics of the etching process, resulting in the loss of Al_2O is shown to be exothermic by -171.44 kcal mol^{-1}. With the possible exception of the transition states involved in the Al_2O loss, which are currently being investigated, the entire PES for the adsorption of molecular oxygen and subsequent etching is entirely exothermic with respect to the reactants.

The second approach is investigating the energetics involved where an Al cluster is exposed to an oxygenated environment. To simplify the system and avoid the spin state issues seen above, oxygen atoms are used instead of oxygen molecules.

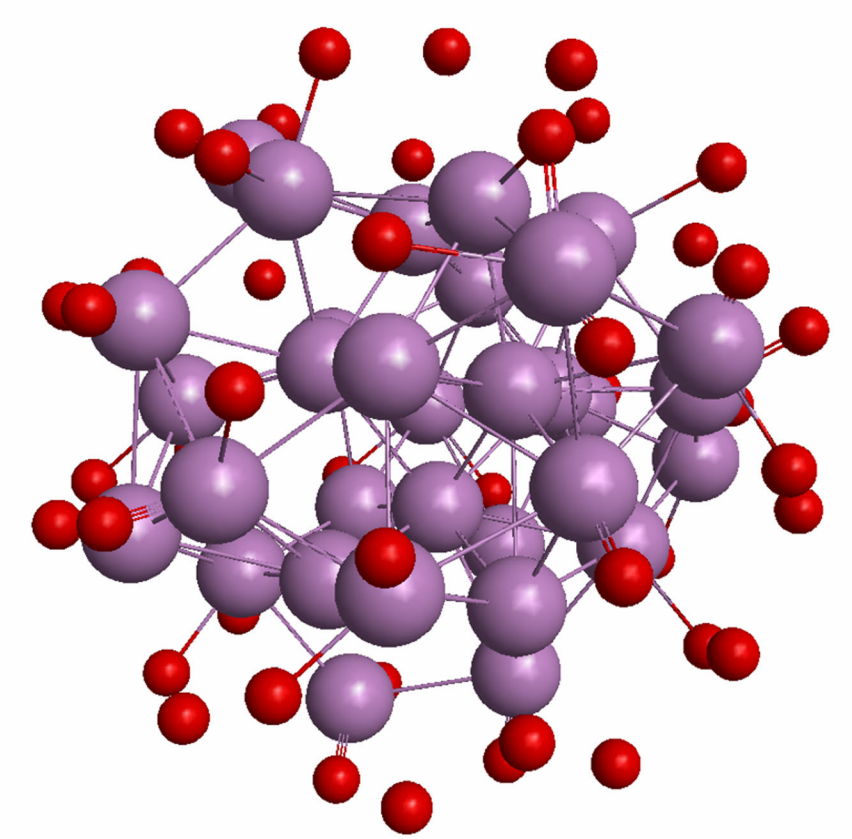

Figure 29. Initial $Al_{32}{\cdot}O_{48}$ structure generated with a "shell" of O atoms via a Fibonacci algorithm set at a radius of 5.8 Å from the CoM of the Al_{32} core.

This is accomplished by having a suitably large Al cluster (Al_{32}) being surrounded by the stochiometrically correct number of oxygen atoms (O_{48}) to form alumina. Initial structures used to optimize the $Al_{32}{\cdot}O_{48}$ clusters are generated systematically. First, from a previously optimized Al_{80} cluster, the center of mass (CoM) is determined and the 32 atoms nearest to the CoM are extracted and reoptimized. The CoM of the subsequently optimized Al_{32} cluster is determined and 48 oxygen atoms are uniformly distributed on the surface of a sphere with radius of 5.8 Å using a three dimensional model of the sunflower, golden spiral or Fibonacci algorithm[45], as illustrated in Figure 29. The subsequently optimized $Al_{32}{\cdot}O_{48}$ cluster is shown in Figure 30, alongside several optimized higher spin states. From this initial starting structure, the most stable structure is a quintet, which is 146.7 kcal mol^{-1} lower than that of the singlet state. Also shown in Figure 30 are the optimized triplet and septet state structures, with respective energies of -105.7 and -112.5 kcal mol^{-1} relative to the singlet state.

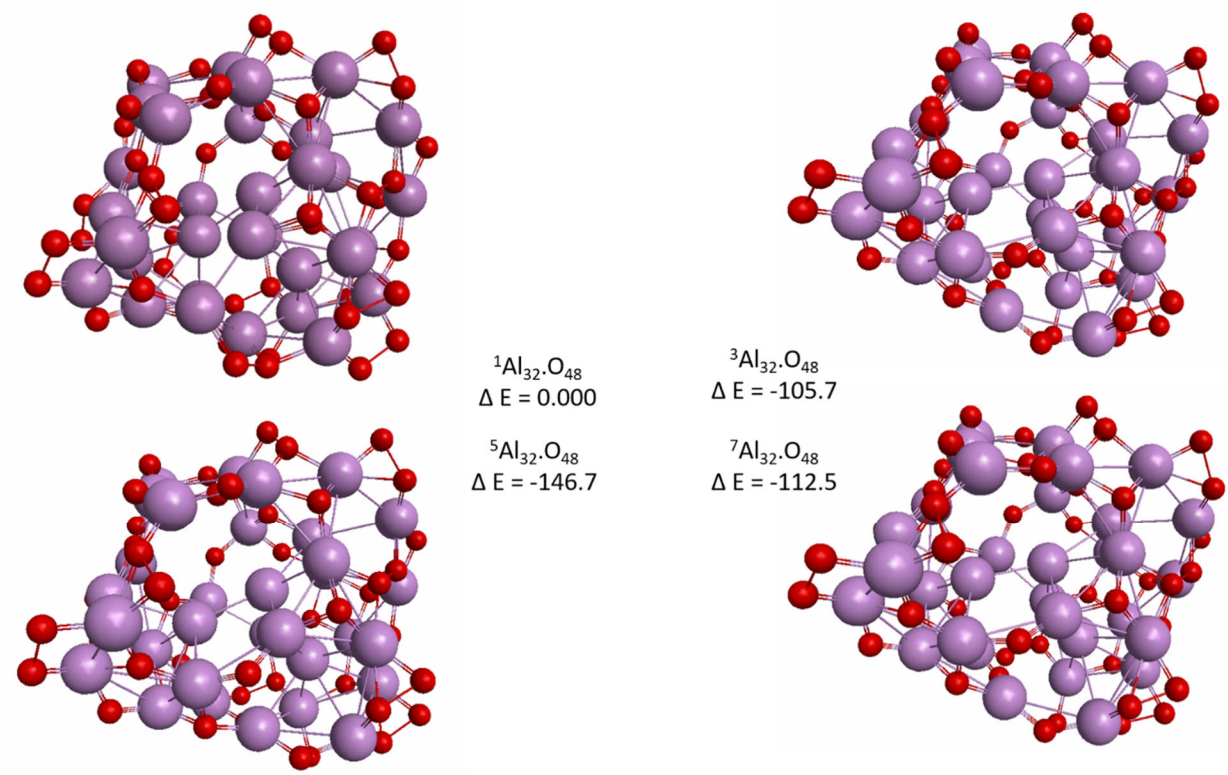

Figure 30. Optimized structures of the singlet, triplet, quintet and septet spin state of the $Al_{32}{\cdot}O_{48}$ cluster. Energies in kcal mol^{-1} with respect to the singlet state energy and include ZPE corrections.

The thermodynamic relative energies involved in oxidative etching via the loss of O_2 and Al_2O are also calculated and can be seen in Figure 31. The process of etching on the singlet surface is entirely exothermic. It begins with a significant drop in energy of 387.88 kcal mol^{-1} through the loss of a single Al_2O from the cluster. From the $Al_{30}{\cdot}O_{47}$ cluster, loss of another Al_2O, forming $Al_{28}{\cdot}O_{46}$, has a barrier of 142.48 kcal mol^{-1}, still well below the energy of the initial structure. However, the PES can continue downhill through the loss of O_2 to form $Al_{30}{\cdot}O_{45}$, with a relative energy of -405.93 with respect to the initial cluster. The remainder of the PES is exothermic with respect to the reactant, up to the formation of $Al_{24}{\cdot}O_{44}$ + 4 Al_2O, which is 318.62 kcal mol^{-1} more stable than $Al_{32}{\cdot}O_{48}$. Because of the significant complexity of this potential energy surface, due to multiple factors such as the size of the system, the plethora of local minima, and the presence of multiple low-lying spin states, a more complete mapping of this surface has not been pursued. However, the results reported in both the Al_{30} + O_2 study and the $Al_{32}{\cdot}O_{48}$ study clearly suggest that oxidative etching of Al nanoclusters is energetically favorable and may be the reason that current experimental synthesis efforts have yielded no detectable clusters.

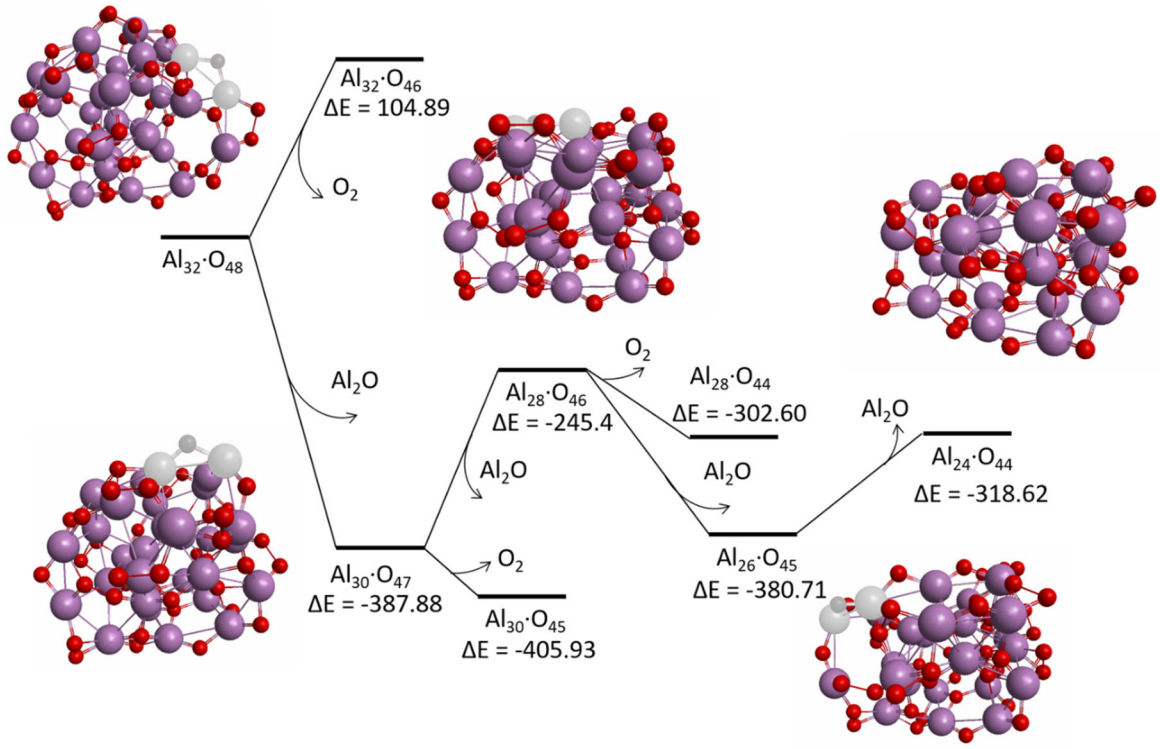

Figure 31. Singlet PES for the oxidative etching of an Al_{32} nanocluster. Grayed atoms depict the surface Al_2O that is removed in the following cluster. Energies in kcal mol^{-1} with respect to $^1Al_{32}{\cdot}O_{48}$.

Limits of chemical storage

Additional work in collaboration with colleagues at Eglin AFB, has been aimed at exploring the fundamental limitations to chemical energy storage, in part by examining how the distances between individual atoms are coupled to the energy stored in the bonds of the molecule. It is well known that stronger molecular bonds pull atoms closer together and thus stronger bonding results in shorter bond lengths. This leads to the fact that the potential minimum for the ground electronic state deepens at shorter intramolecular distances. To illustrate this point, consider a slice through the multidimensional potential energy surface along a carbon-oxygen or carbon-carbon bonding coordinate for molecules with single, double, and triple bonds. Figure 32 depicts examples of these one-dimensional potential energy surfaces (PES) for several simple polyatomic molecules. These PESs have been constructed by initially optimizing the geometry of the species using the multi-configuration self-consistent field (MCSCF)[46-48] theory, using the augmented correlation consistent polarized valence triple zeta (aug-cc-pVTZ) basis set[49, 50], thereby locating the minimum energy well of the CC or CO potential energy surface. This was followed by constrained optimizations in which the distance of the dissociating CC or CO bond is frozen while the remaining structure is allowed to relax. This is repeated systematically at both increasing and decreasing increments from the initial local minima to obtain the potential energy curve. To achieve more accurate energies of these potentials, Multi Reference second order

Moller-Plesset perturbation theory (MRMP2)[51-54] single point energy calculations are applied at each point along the PES with the same active space[1].

These potentials show that the associated equilibrium bond length decreases and the bond dissociation energy increases (*i.e.* the depth of the well) as the bond order increases from single to triple bonds. In both the carbon-carbon and carbon-oxygen bonding potentials, the trends are very similar. The equilibrium bond lengths appear to vary linearly with the well depths over the range of equilibrium bond lengths explored here.

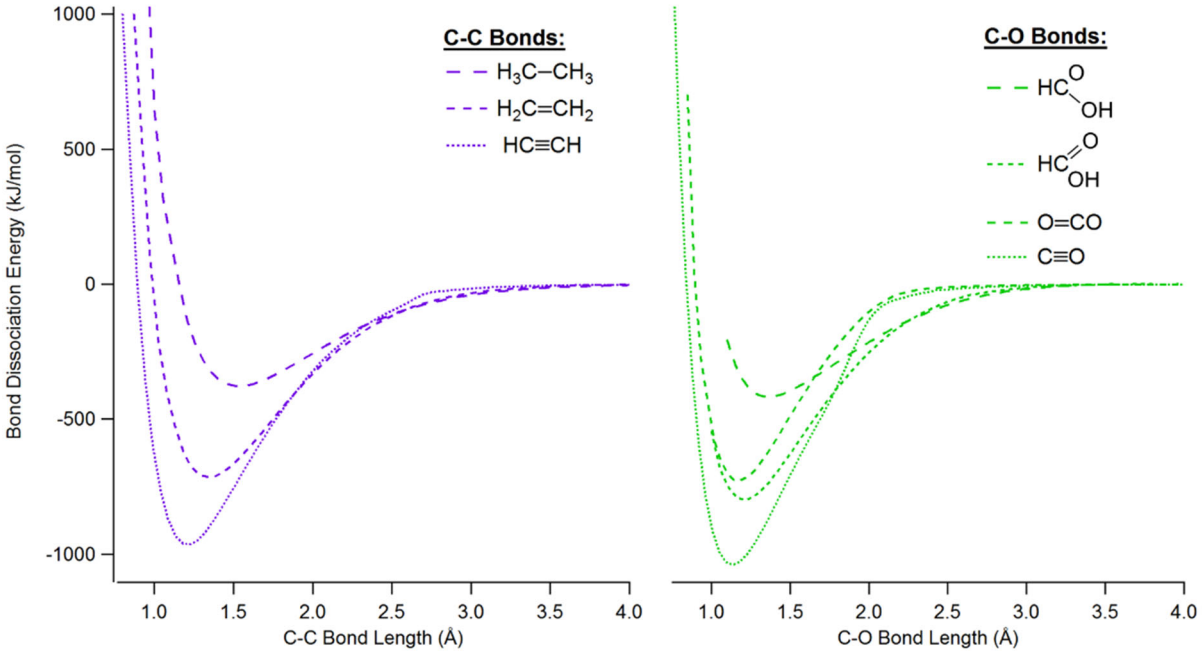

Figure 32. Reduced adiabatic potential energy surfaces along the carbon-carbon (left) and carbon-oxygen (right) bonding coordinates for several different bonding orders. As the depth of each bonding well increases, the equilibrium bond length shortens. These potentials are calculated at the MCSCF/MRMP2 level of theory with aug-cc-pVTZ basis sets.[a]

Looking deeper into this notion, homolytic bond dissociation energies for a wide range of carbon, nitrogen, and oxygen-containing covalent bonds were computed at the MP2/aug-cc-PVTZ level of theory. As shown in Table 2, over 40 different molecules with internal bond lengths ranging from 1.20 to 1.71 Å were considered. All open shell species were computed using a restricted open shell (ROHF) wave function, with the exception of the phenoxy and C_7H_5 radicals which were computed using an unrestricted (UHF) wave function. This was done due to

[a] The MCSCF orbital active spaces used are as follows: CH_3-CH_3 (2e, 2o); C-C σ, σ*; CH_2=CH_2 (12e,12o); full valence; HC≡CH (10e,10); full valence; OCH-OH (2e,2o); C-O σ, σ*; O=CHOH (4e,4o); C-O σ, σ*, π, π*; O=CO (12e,10o); full valence, excluding O 2s

difficulties in converging the ROHF wavefunction, presumably due to the high spin contamination present in these species.

Several of the systems considered here adiabatically dissociate into an excited electronic state, particularly in the case where a double or triple bond is broken. . For example, homolytic dissociation of a C=O bond in OCO adiabatically can lead to formation of singlet CO and singlet O or triplet CO plus triplet O, whereas of course the ground states of CO and O are a singlet and triplet, respectively. In such cases, the relative energies of both the ground state and an adiabatic asymptote are highlighted in Table 2.

Table 2. Bond dissociation Energies for various N-N, O-O, C-O, C-N, and C-C Bonds @ MP2/aug-cc-pVTZ

"Adiabatic" RXN	"Adiabatic" BDE (kJ/mol)	Bond Length (Å)	"Relaxed" BDE (kJ/mol)	"Relaxed" RXN
N-N Bonding				
$N_2 \rightarrow {}^4N + {}^4N$	978.2	1.114	978.2	$N_2 \rightarrow {}^4N + {}^4N$
$N_2H_4 \rightarrow {}^2NH_2 + {}^2NH_2$	286.8	1.434	286.8	$N_2H_4 \rightarrow {}^2NH_2 + {}^2NH_2$
$N_2F_4 \rightarrow {}^2NF_2 + {}^2NF_2$	111.8	1.501	111.8	$N_2F_4 \rightarrow {}^2NF_2 + {}^2NF_2$
$N_3H \rightarrow {}^3N_2 + {}^3NH$	786.7	1.243	92.6	$N_3H \rightarrow N_2 + {}^3NH$
$N_3H \rightarrow {}^4HN_2 + {}^4N$	1012.6	1.146	478.3	$N_3H \rightarrow {}^2HN_2 + {}^4N$
$N_2O \rightarrow {}^4NO + {}^4N$	1036.4	1.155	528.6	$N_2O \rightarrow {}^2NO + {}^4N$
$N_2O_2 \rightarrow {}^2NO + {}^2NO$	13.2	2.189	13.2	$N_2O_2 \rightarrow {}^2NO + {}^2NO$
$N_2O_3 \rightarrow {}^2NO_2 + {}^2NO$	43.4	1.886	43.4	$N_2O_3 \rightarrow {}^2NO_2 + {}^2NO$
$N_2O_4 \rightarrow {}^2NO_2 + {}^2NO_2$	74.5	1.821	74.5	$N_2O_4 \rightarrow {}^2NO_2 + {}^2NO_2$
$N_2(CH_3)_2 \rightarrow {}^3N(CH_3) + {}^3N(CH_3)$	526.8	1.250	23.1	$N_2(CH_3)_2 \rightarrow {}^1N(CH_3) + {}^1N(CH_3)$
$N_2(CH_2CH_3)_2 \rightarrow {}^3N(CH_2CH_3) + {}^3N(CH_2CH_3)$	541.7	1.251	66.2	$N_2(CH_2CH_3)_2 \rightarrow {}^1N(CH_2CH_3) + {}^1N(CH_2CH_3)$
$N_2(C_6H_5)_2 \rightarrow {}^3N(C_6H_5) + {}^3N(C_6H_5)$	494.5	1.263	494.5	$N_2(C_6H_5)_2 \rightarrow {}^3N(C_6H_5) + {}^3N(C_6H_5)$
cis-$N_2[H,CH_3]_2 \rightarrow {}^2N[H,CH_3] + {}^2N[H,CH_3]$	289.3	1.428	289.3	cis-$N_2[H,CH_3]_2 \rightarrow {}^2N[H,CH_3] + {}^2N[H,CH_3]$
trans-$N_2[H,CH_3]_2 \rightarrow {}^2N[H,CH_3] + {}^2N[H,CH_3]$	289.3	1.428	289.3	trans-$N_2[H,CH_3]_2 \rightarrow {}^2N[H,CH_3] + {}^2N[H,CH_3]$
$N_2H_2O_2 \rightarrow {}^2H_2N + {}^2NO_2$	212.6	1.392	212.6	$N_2H_2O_2 \rightarrow {}^2H_2N + {}^2NO_2$
$N_2CH_4O_2 \rightarrow {}^2N[H,CH_3] + {}^2NO_2$	219.6	1.381	219.6	$N_2CH_4O_2 \rightarrow {}^2N[H,CH_3] + {}^2NO_2$
$N_2CH_2O_2 \rightarrow {}^2NCH_2 + {}^2NO_2$	148.2	1.454	148.2	$N_2CH_2O_2 \rightarrow {}^2NCH_2 + {}^2NO_2$
$N_2H_2O \rightarrow {}^3NH + {}^3HNO$	459.0	1.280	375.2	$N_2H_2O \rightarrow {}^3NH + {}^1HNO$
$N_2CH_4O \rightarrow {}^3NH + {}^3N[O,CH_3]$	469.6	1.283	369.9	$N_2CH_4O \rightarrow {}^3NH + {}^1N[O,CH_3]$
$N_2H_2O_2 \rightarrow {}^3HNO + {}^3HNO$	277.2	1.343	109.5	$N_2H_2O_2 \rightarrow {}^1HNO + {}^1HNO$
$N_2C_2H_6O_2 \rightarrow {}^3N[O,CH_3] + {}^3N[O,CH_3]$	318.9	1.345	119.6	$N_2C_2H_6O_2 \rightarrow {}^1N[O,CH_3] + {}^1N[O,CH_3]$
O-O Bonding				
$^3O_2 \rightarrow {}^3O + {}^3O$	570.7	1.241	570.7	$^3O_2 \rightarrow {}^3O + {}^3O$
$^2HO_2 \rightarrow {}^2OH + {}^3O$	269.5	1.310	269.5	$^2HO_2 \rightarrow {}^2OH + {}^3O$
$H_2O_2 \rightarrow {}^2OH + {}^2OH$	229.0	1.454	229.0	$H_2O_2 \rightarrow {}^2OH + {}^2OH$
$^2FO_2 \rightarrow {}^3O + {}^2OF$	348.0	1.131	348.0	$^2FO_2 \rightarrow {}^3O + {}^2OF$
$F_2O_2 \rightarrow {}^2OF + {}^2OF$	223.9	1.166	223.9	$F_2O_2 \rightarrow {}^2OF + {}^2OF$
$O_3 \rightarrow {}^3O_2 + {}^3O$	109.5	1.284	109.5	$O_3 \rightarrow {}^3O_2 + {}^3O$

$CH_4O_2 \rightarrow {}^2CH_3O + {}^2OH$	217.5	1.456	217.5	$CH_4O_2 \rightarrow {}^2CH_3O + {}^2OH$
$C_2H_6O_2 \rightarrow {}^2C_2H_5O + {}^2OH$	219.1	1.458	219.1	$C_2H_6O_2 \rightarrow {}^2C_2H_5O + {}^2OH$
$C_6H_6O_2 \rightarrow {}^2C_6H_5O + {}^2OH$	224.6	1.447	224.6	$C_6H_6O_2 \rightarrow {}^2C_6H_5O + {}^2OH$
$C_2H_6O_2 \rightarrow {}^2CH_3O + {}^2CH_3O$	208.8	1.465	208.8	$C_2H_6O_2 \rightarrow {}^2CH_3O + {}^2CH_3O$
$C_2H_6O_2 \rightarrow {}^2CH_3O + {}^2CH_3O$	214.0	1.464	214.0	$C_2H_6O_2 \rightarrow {}^2CH_3O + {}^2CH_3O$
$C_{12}H_{10}O_2 \rightarrow {}^2C_6H_5O + {}^2C_6H_5O$	223.6	1.453	223.6	$C_{12}H_{10}O_2 \rightarrow {}^2C_6H_5O + {}^2C_6H_5O$
C-O Bonding				
$CO \rightarrow {}^3C + {}^3O$	1111.0	1.139	1111.0	$CO \rightarrow {}^3C + {}^3O$
$CO_2 \rightarrow {}^3CO + {}^3O$	1162.0	1.170	570.0	$CO_2 \rightarrow CO + {}^3O$
$OCS \rightarrow {}^3CS + {}^3O$	1073.5	1.169	717.0	$OCS \rightarrow CS + {}^3O$
$^2OCN \rightarrow {}^4CN + {}^3O$	1120.1	1.175	569.5	$^2OCN \rightarrow {}^2CN + {}^3O$
$^2HCO \rightarrow {}^4CH + {}^3O$	895.8	1.182	842.6	$^2HCO \rightarrow {}^2CH + {}^3O$
$^2CH_3O \rightarrow {}^2CH_3 + {}^3O$	369.2	1.378	369.2	$^2CH_3O \rightarrow {}^2CH_3 + {}^3O$
$HCOOH \rightarrow {}^2HCO + {}^2OH$	455.2	1.354	455.2	$HCOOH \rightarrow {}^2HCO + {}^2OH$
$HCOOH \rightarrow {}^3HCOH + {}^3O$	876.6	1.199	757.4	$HCOOH \rightarrow {}^1HCOH + {}^3O$
$C_2H_3OOH \rightarrow {}^2C_2H_3O + {}^2OH$	455.4	1.364	455.4	$C_2H_3OOH \rightarrow {}^2C_2H_3O + {}^2OH$
$C_2H_3OOH \rightarrow {}^3C_2H_3OH + {}^3O$	874.8	1.204	742.6	$C_2H_3OOH \rightarrow {}^1C_2H_3OH + {}^3O$
$C_3H_5OOH \rightarrow {}^2C_3H_5O + {}^2OH$	458.0	1.364	458.0	$C_3H_5OOH \rightarrow {}^2C_3H_5O + {}^2OH$
$C_3H_5OOH \rightarrow {}^3C_3H_5OH + {}^3O$	879.9	1.204	747.9	$C_3H_5OOH \rightarrow {}^1C_3H_5OH + {}^3O$
$C_7H_5OOH \rightarrow {}^2C_7H_5O + {}^2OH$	481.7	1.359	481.7	$C_7H_5OOH \rightarrow {}^2C_7H_5O + {}^2OH$
$C_7H_5OOH \rightarrow {}^3C_7H_5OH + {}^3O$	855.8	1.207	733.7	$C_7H_5OOH \rightarrow {}^1C_7H_5OH + {}^3O$
$H_2CO \rightarrow {}^3CH_2 + {}^3O$	774.4	1.213	774.4	$H_2CO \rightarrow {}^3CH_2 + {}^3O$
$C_3H_6O \rightarrow {}^3C_3H_6 + {}^3O$	819.7	1.220	810.4	$C_3H_6O \rightarrow {}^1C_3H_6 + {}^3O$
$C_{13}H_{10}O \rightarrow {}^3C_{13}H_{10} + {}^3O$	788.2	1.227	769.0	$C_{13}H_{10}O \rightarrow {}^1C_{13}H_{10} + {}^3O$
$C_4H_8O \rightarrow {}^3C_4H_8 + {}^3O$	824.4	1.220	805.4	$C_4H_8O \rightarrow {}^1C_4H_8 + {}^3O$
$C_2H_6O \rightarrow {}^2CH_3O + {}^2CH_3$	378.3	1.412	378.3	$C_2H_6O \rightarrow {}^2CH_3O + {}^2CH_3$
$C_4H_{10}O \rightarrow {}^2C_2H_5O + {}^2C_2H_5$	395.9	1.417	395.9	$C_4H_{10}O \rightarrow {}^2C_2H_5O + {}^2C_2H_5$
$C_6H_{14}O \rightarrow {}^2C_3H_7O + {}^2C_3H_7$	399.0	1.416	399.0	$C_6H_{14}O \rightarrow {}^2C_3H_7O + {}^2C_3H_7$
$C_{14}H_{14}O \rightarrow {}^2C_7H_7O + {}^2C_7H_7$	364.1	1.418	364.1	$C_{14}H_{14}O \rightarrow {}^2C_7H_7O + {}^2C_7H_7$
$C_3H_8O \rightarrow {}^2C_2H_5O + {}^2CH_3$	375.5	1.414	375.5	$C_3H_8O \rightarrow {}^2C_2H_5O + {}^2CH_3$
$C_3H_8O \rightarrow {}^2CH_3O + {}^2C_2H_5$	386.7	1.420	386.7	$C_3H_8O \rightarrow {}^2CH_3O + {}^2C_2H_5$
$CH_3OH \rightarrow {}^2CH_3 + {}^2OH$	399.8	1.424	399.8	$CH_3OH \rightarrow {}^2CH_3 + {}^2OH$
$C_2H_5OH \rightarrow {}^2C_2H_5 + {}^2OH$	411.7	1.427	411.7	$C_2H_5OH \rightarrow {}^2C_2H_5 + {}^2OH$
$C_6H_5OH \rightarrow {}^2C_6H_5 + {}^2OH$	496.9	1.370	496.9	$C_6H_5OH \rightarrow {}^2C_6H_5 + {}^2OH$
$t\text{-}C_3H_7OH \rightarrow {}^2C_3H_7 + {}^2OH$	421.5	1.432	421.5	$t\text{-}C_3H_7OH \rightarrow {}^2C_3H_7 + {}^2OH$
$C_3H_7OH \rightarrow {}^2C_3H_7 + {}^2OH$	415.8	1.427	415.8	$C_3H_7OH \rightarrow {}^2C_3H_7 + {}^2OH$
$C_4H_9OH \rightarrow {}^2C_4H_9 + {}^2OH$	429.5	1.438	429.5	$C_4H_9OH \rightarrow {}^2C_4H_9 + {}^2OH$
C-N Bonding				
$CN \rightarrow {}^5C + {}^4N$	1116.2	1.190	761.3	$CN \rightarrow {}^3C + {}^4N$
$CH_3NH_2 \rightarrow {}^2CH_3 + {}^2NH_2$	362.0	1.464	362.0	$CH_3NH_2 \rightarrow {}^2CH_3 + {}^2NH_2$
$C_2H_5NH_2 \rightarrow {}^2C_2H_5 + {}^2NH_2$	370.3	1.465	370.3	$C_2H_5NH_2 \rightarrow {}^2C_2H_5 + {}^2NH_2$
$C_6H_5NH_2 \rightarrow {}^2C_6H_5 + {}^2NH_2$	462.5	1.400	462.5	$C_6H_5NH_2 \rightarrow {}^2C_6H_5 + {}^2NH_2$

$CH_3NO_2 \rightarrow {}^2CH_3 + {}^2NO_2$	246.6	1.485	246.6	$CH_3NO_2 \rightarrow {}^2CH_3 + {}^2NO_2$
$C_2H_5NO_2 \rightarrow {}^2C_2H_5 + {}^2NO_2$	243.6	1.489	243.6	$C_2H_5NO_2 \rightarrow {}^2C_2H_5 + {}^2NO_2$
$C_6H_5NO_2 \rightarrow {}^2C_6H_5 + {}^2NO_2$	320.2	1.470	320.2	$C_6H_5NO_2 \rightarrow {}^2C_6H_5 + {}^2NO_2$
$HCN \rightarrow {}^4CH + {}^4N$	981.7	1.167	981.7	$HCN \rightarrow {}^4CH + {}^4N$
$HC_3N \rightarrow {}^4C_3H + {}^4N$	1027.4	1.177	1027.4	$HC_3N \rightarrow {}^4C_3H + {}^4N$
$C_2H_3N \rightarrow {}^4C_2H_3 + {}^4N$	1070.4	1.170	944.8	$C_2H_3N \rightarrow {}^2C_2H_3 + {}^4N$
$C_3H_5N \rightarrow {}^4C_3H_5 + {}^4N$	1071.3	1.171	949.5	$C_3H_5N \rightarrow {}^2C_3H_5 + {}^4N$
$C_7H_5N \rightarrow {}^4C_7H_5 + {}^4N$	1137.7	1.174	954.0	$C_7H_5N \rightarrow {}^2C_7H_5 + {}^4N$
C-C Bonding				
$C_{38}H_{30} \rightarrow {}^2C_{19}H_{15} + {}^2C_{19}H_{15}$				$C_{38}H_{30} \rightarrow {}^2C_{19}H_{15} + {}^2C_{19}H_{15}$
$C_2Cl_6 \rightarrow {}^2CCl_3 + {}^2CCl_3$	352.3	1.574	352.3	$C_2Cl_6 \rightarrow {}^2CCl_3 + {}^2CCl_3$
$C_2H_6 \rightarrow {}^2CH_3 + {}^2CH_3$	378.8	1.524	378.8	$C_2H_6 \rightarrow {}^2CH_3 + {}^2CH_3$
$C_4H_4 \rightarrow {}^2C_2H_3 + {}^2C_2H$	604.0	1.424	604.0	$C_4H_4 \rightarrow {}^2C_2H_3 + {}^2C_2H$
$C_4H_2 \rightarrow {}^2C_2H + {}^2C_2H$	714.2	1.369	714.2	$C_4H_2 \rightarrow {}^2C_2H + {}^2C_2H$
$C_2H_4 \rightarrow {}^3CH_2 + {}^3CH_2$	729.8	1.333	729.8	$C_2H_4 \rightarrow {}^3CH_2 + {}^3CH_2$
$C_2H_2 \rightarrow {}^4CH + {}^4CH$	898.9	1.299	792.6	$C_2H_2 \rightarrow {}^2CH + {}^2CH$

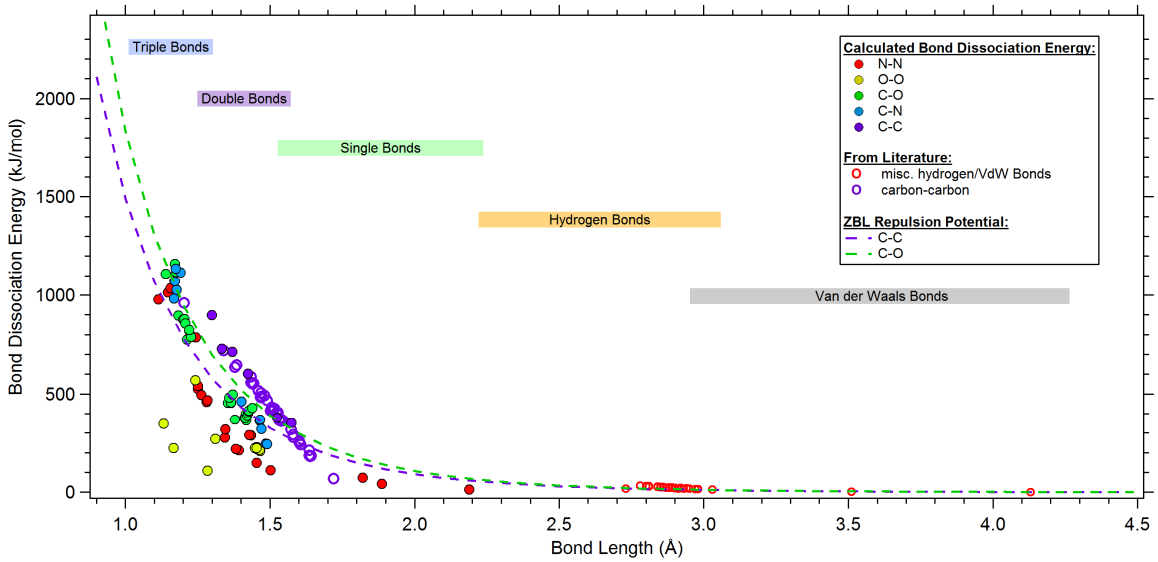

Figure 33. Calculated homolytic bond dissociation energies as a function of equilibrium bond lengths for various carbon, oxygen, and nitrogen covalent bonds (solid markers) as well as additional representative covalent, hydrogen and Van der Waals bonds reported elsewhere[55, 56] (open markers). Remarkably, a simple trend emerges across a very wide range of bonding motifs, strengths and lengths. This general trend suggests that the behavior is predominantly driven by nuclear repulsion and can be illustrated by overlaying the nuclear repulsion energy as estimated using the Zielger, Biersack, and Littmark[55] shielded potential (dashed lines).

Figure 33 summarizes the results of these calculations which extends the trends observed in Zavitsas' work[57] as well as those observed in Figure 32. When looking at a larger range of bond lengths it is clear that the relationship between bond dissociation energy and bond length is not

linear, but an increasingly steep inverse relationship as the bond shortens. Within each class of bonds there seems to be a tighter relationship with only a few exceptions. What is perhaps most intriguing is that the same trend exists across a diverse set of molecular compounds, bonding motifs, and bonding types, suggesting that the primary cause is something more fundamental and simpler than the complexity of each system's valence electronic structure.

Summary

The primary objectives of this LRIR are to predict key properties of core-shell-nanoclusters, such as the ability to synthesize these species utilizing HDMD and understanding the chemistry involved in this process. More specifically, these objectives include understanding the (a) structure and energetics of Al core-shell nanoclusters, (b) the propensity for structural inversion of such core-shell species, and (c) the energetics of oxidation and etching of aluminum nanoclusters.

It is clear from the calculations presented herein that gold, copper, and silicon bind strongly to aluminum and therefore are capable of coating the aluminum surface to initially form a core-shell nanocluster. The predicted binding energies of two atoms bound to the Al_{30} nanocluster surface range from 133-169 (gold), 121-151 (copper), and 168-192 (silicon) kcal mol^{-1}, respectively. The calculations show that gold preferentially binds to aluminum nanoclusters as two individual atoms rather than as a diatom. In the case of copper and silicon, the energetic preference of atoms versus diatomics for attachment to the nanocluster is less clear.

In investigating the structural inversion energetics of Al core-shell nanoclusters, it is found that the details of the interactions between the cluster and surface atoms in general are sensitive to the initial placement of the surface atoms on the cluster. While the energetic profiles of gold atoms migrating into the interior of Al_{30} are similar (Figure 17), they are mechanistically very different with respect to the interactions with the three interior Al atoms. This set of calculations indicates that although gold atoms strongly bind to the Al cluster surface, it is energetically unfavorable for the gold atoms to become fully encapsulated within the cluster interior, suggesting in turn that gold-coated aluminum nanoclusters should be structurally stable and unlikely to undergo inversion. In contrast, the complementary system with two aluminum atoms on the surface of an Au_{30} nanocluster, shows little or no barrier to aluminum entering the cluster interior (Figure 18). This implies that aluminum-coated gold nanoclusters are intrinsically unstable and therefore capable of undergoing an inversion process.

The Al/Si system $Al_{30}{\cdot}Si_2$, with two Si atoms initially on the surface of Al_{30}, shows distinct energy profiles as a function of initial positions of the silicon atoms. As shown in Figure 22, all three PESs show an initial increase in ΔE at the outset as the surface Si atoms are forced closer together. While all points along two of the energy profiles are less stable than the initial nanocluster, the third profile includes multiple structures in which an embedded Si atom is more stable than when on the Al_{30} surface. Therefore, to the extent that the initial energy barrier of ~6

kcal mol^{-1} at R(Si-Si)≈9 Å inhibits encapsulation of silicon atoms on the cluster surface, silicon-coated aluminum core-shell nanoclusters are predicted to be metastable under the cryogenic conditions of the HDMD experiments. In the complementary system $Si_{30}{\cdot}Al_2$, with two aluminum atoms initially on the surface of a Si_{30} cluster, full encapsulation of an aluminum atom within the Si_{30} interior is a highly exothermic process, as illustrated in Figure 26. Nonetheless, intervening barriers of ~5 to ~15 kcal mol^{-1} suggest that aluminum-coated silicon nanoclusters may be metastable, though perhaps more likely to undergo structural inversion than the silicon-coated aluminum counterparts.

Oxidative processes are anticipated to play important roles in the formation, structural modifications (i.e., inversion), and agglomeration of core-shell nanoparticles. Therefore, the mechanisms and energetics of aluminum nanocluster oxidation and etching have been investigated. The oxidative etching of Al clusters is studied from two different perspectives. First is the oxidation of an Al_{30} cluster via a single oxygen molecule, in which it was shown that with the possible exception of the transition states involved in the loss of Al_2O, the entire PES for the adsorption of molecular oxygen and subsequent etching is entirely exothermic with respect to the reactants, and has an overall exothermicity of 171 kcal mol^{-1}. The second approach involved a stoichiometrically oxidized Al cluster ($Al_{32}{\cdot}O_{48}$) and subsequent etching modeled via the loss of O_2 and Al_2O. A pathway was identified in which the entire process of etching on the singlet surface is exothermic, suggesting that oxidative etching of Al nanoclusters is energetically favorable, as expected.

In addition, a series of calculations designed to investigate the fundamental limits of chemical energy storage based upon chemical bond lengths and bond energies is summarized. When looking over a broad range of bond lengths it is clear that the relationship between bond dissociation energy and bond length is not linear, but an increasingly steep inverse relationship as the bond shortens. Within each class of bonds (N-N, O-O, C-O, etc.) there seems to be a tighter relationship with only a few exceptions. What is perhaps most intriguing is that the same trend exists across a diverse set of molecular compounds, bonding motifs, and bonding types, suggesting that the primary cause is something more fundamental and simpler than the complexity of each system's valence electronic structure.

References

1. Emery, S. B.; Boyle, J. M.; Rider, K. B.; Little, B. K.; Lindsay, C. M., Nano-scale energetic films by superfluid helium droplet assembly. In *18th Aps-Sccm and 24th Airapt, Pts 1-19*, Buttler, W.; Furlanetto, M.; Evans, W., Eds. 2014; Vol. 500.
2. Mozhayskiy, V.; Slipchenko, M. N.; Adamchuk, V. K.; Vilesov, A. F., Use of helium nanodroplets for assembly, transport, and surface deposition of large molecular and atomic clusters. *J. Chem. Phys.* **2007,** *127* (9).
3. Gomez, L. F.; Loginov, E.; Vilesov, A. F., Traces of Vortices in Superfluid Helium Droplets. *Phys. Rev. Lett.* **2012,** *108* (15).
4. Loginov, E.; Gomez, L. F.; Vilesov, A. F., Surface Deposition and Imaging of Large Ag Clusters Formed in He Droplets. *J. Phys. Chem. A* **2011,** *115* (25), 7199-7204.
5. Boatwright, A.; Feng, C.; Spence, D.; Latimer, E.; Binns, C.; Ellis, A. M.; Yang, S., Helium droplets: a new route to nanoparticles. *Faraday Discuss.* **2013,** *162*, 113-124.
6. Volk, A.; Thaler, P.; Koch, M.; Fisslthaler, E.; Grogger, W.; Ernst, W. E., High resolution electron microscopy of Ag-clusters in crystalline and non-crystalline morphologies grown inside superfluid helium nanodroplets. *J. Chem. Phys.* **2013,** *138* (21).
7. Thaler, P.; Volk, A.; Lackner, F.; Steurer, J.; Knez, D.; Grogger, W.; Hofer, F.; Ernst, W. E., Formation of bimetallic core-shell nanowires along vortices in superfluid He nanodroplets. *Phys. Rev. B* **2014,** *90* (15).
8. Spence, D.; Latimer, E.; Feng, C.; Boatwright, A.; Ellis, A. M.; Yang, S., Vortex-induced aggregation in superfluid helium droplets. *Phys. Chem. Chem. Phys.* **2014,** *16* (15), 6903-6906.
9. Cleaver, R. M.; Lindsay, C. M., Detailed design and transport properties of a helium droplet nozzle from 5 to 50 K. *Cryogenics* **2012,** *52* (7-9), 389-397.
10. McMahon, B. W.; Yu, J.; Boatz, J. A.; Anderson, S. L., Rapid Aluminum Nanoparticle Production by Milling in NH3 and CH3NH2 Atmospheres: An Experimental and Theoretical Study. *Acs Applied Materials & Interfaces* **2015,** *7* (29), 16101-16116.
11. Perez, J. P. L.; McMahon, B. W.; Yu, J.; Schneider, S.; Boatz, J. A.; Hawkins, T. W.; McCrary, P. D.; Flores, L. A.; Rogers, R. D.; Anderson, S. L., Boron Nanoparticles with High Hydrogen Loading: Mechanism for B-H Binding and Potential for Improved Combustibility and Specific Impulse. *Acs Applied Materials & Interfaces* **2014,** *6* (11), 8513-8525.
12. Yu, J.; Boatz, J. A.; Tang, X.; Hicks, Z. A.; Bowen, K. H.; Anderson, S. L., Borane-Aluminum Surface Interactions: Enhanced Fracturing and Generation of Boron-Aluminum Core-Shell Nanoparticles. *Journal of Physical Chemistry C* **2017,** *121* (26), 14176-14190.
13. Yu, J.; McMahon, B. W.; Boatz, J. A.; Anderson, S. L., Aluminum Nanoparticle Production by Acetonitrile-Assisted Milling: Effects of Liquid- vs Vapor-Phase Milling and of Milling Method on Particle Size and Surface Chemistry. *Journal of Physical Chemistry C* **2016,** *120* (35), 19613-19629.
14. Becke, A. D., DENSITY-FUNCTIONAL THERMOCHEMISTRY .3. THE ROLE OF EXACT EXCHANGE. *J. Chem. Phys.* **1993,** *98* (7), 5648-5652.
15. Lee, C. T.; Yang, W. T.; Parr, R. G., DEVELOPMENT OF THE COLLE-SALVETTI CORRELATION-ENERGY FORMULA INTO A FUNCTIONAL OF THE ELECTRON-DENSITY. *Phys. Rev. B* **1988,** *37* (2), 785-789.
16. Miehlich, B.; Savin, A.; Stoll, H.; Preuss, H., RESULTS OBTAINED WITH THE CORRELATION-ENERGY DENSITY FUNCTIONALS OF BECKE AND LEE, YANG AND PARR. *Chem. Phys. Lett.* **1989,** *157* (3), 200-206.
17. Burke, K.; Perdew, J. P.; Ernzerhof, M., Mixing exact exchange with GGA: When to say when. *Electronic Density Functional Theory: Recent Progress and New Directions* **1998**, 57-68.

18. Perdew, J. P., In *Electronic Structures of Solids '91*, Akademie Verlag: Berlibn, 1991; p 11.
19. Perdew, J. P.; Burke, K.; Wang, Y., Generalized gradient approximation for the exchange-correlation hole of a many-electron system. *Phys. Rev. B* **1996,** *54* (23), 16533-16539.
20. Perdew, J. P.; Chevary, J. A.; Vosko, S. H.; Jackson, K. A.; Pederson, M. R.; Singh, D. J.; Fiolhais, C., ATOMS, MOLECULES, SOLIDS, AND SURFACES - APPLICATIONS OF THE GENERALIZED GRADIENT APPROXIMATION FOR EXCHANGE AND CORRELATION. *Phys. Rev. B* **1992,** *46* (11), 6671-6687.
21. Perdew, J. P.; Chevary, J. A.; Vosko, S. H.; Jackson, K. A.; Pederson, M. R.; Singh, D. J.; Fiolhais, C., ATOMS, MOLECULES, SOLIDS, AND SURFACES - APPLICATIONS OF THE GENERALIZED GRADIENT APPROXIMATION FOR EXCHANGE AND CORRELATION (VOL 46, PG 6671, 1992). *Phys. Rev. B* **1993,** *48* (7), 4978-4978.
22. Perdew, J. P.; Burke, K.; Ernzerhof, M., Generalized gradient approximation made simple (vol 77, pg 3865, 1996). *Phys. Rev. Lett.* **1997,** *78* (7), 1396-1396.
23. Perdew, J. P.; Burke, K.; Ernzerhof, M., Generalized gradient approximation made simple. *Phys. Rev. Lett.* **1996,** *77* (18), 3865-3868.
24. Frisch, M. J.; Headgordon, M.; Pople, J. A., A DIRECT MP2 GRADIENT-METHOD. *Chem. Phys. Lett.* **1990,** *166* (3), 275-280.
25. Pople, J. A.; Binkley, J. S.; Seeger, R., THEORETICAL MODELS INCORPORATING ELECTRON CORRELATION. *International Journal of Quantum Chemistry* **1976**, 1-19.
26. Aikens, C. M.; Fletcher, G. D.; Schmidt, M. W.; Gordon, M. S., Scalable implementation of analytic gradients for second-order Z-averaged perturbation theory using the distributed data interface. *J. Chem. Phys.* **2006,** *124* (1).
27. Piecuch, P.; Kucharski, S. A.; Kowalski, K.; Musial, M., Efficient computer implementation of the renormalized coupled-cluster methods: The R-CCSD T , R-CCSD(T), CR-CCSD T , and CR-CCSD(T) approaches. *Computer Physics Communications* **2002,** *149* (2), 71-96.
28. Piecuch, P.; Wloch, M., Renormalized coupled-cluster methods exploiting left eigenstates of the similarity-transformed Hamiltonian. *J. Chem. Phys.* **2005,** *123* (22).
29. Stevens, W. J.; Basch, H.; Krauss, M., COMPACT EFFECTIVE POTENTIALS AND EFFICIENT SHARED-EXPONENT BASIS-SETS FOR THE 1ST-ROW AND 2ND-ROW ATOMS. *J. Chem. Phys.* **1984,** *81* (12), 6026-6033.
30. Stevens, W. J.; Krauss, M.; Basch, H.; Jasien, P. G., RELATIVISTIC COMPACT EFFECTIVE POTENTIALS AND EFFICIENT, SHARED-EXPONENT BASIS-SETS FOR THE 3RD-ROW, 4TH-ROW, AND 5TH-ROW ATOMS. *Canadian Journal of Chemistry-Revue Canadienne De Chimie* **1992,** *70* (2), 612-630.
31. Schmidt, M. W.; Baldridge, K. K.; Boatz, J. A.; Elbert, S. T.; Gordon, M. S.; Jensen, J. H.; Koseki, S.; Matsunaga, N.; Nguyen, K. A.; Su, S. J.; Windus, T. L.; Dupuis, M.; Montgomery, J. A., GENERAL ATOMIC AND MOLECULAR ELECTRONIC-STRUCTURE SYSTEM. *Journal of Computational Chemistry* **1993,** *14* (11), 1347-1363.
32. Gordon, M. S.; Schmidt, M. W., Advances in electronic structure theory: GAMESS a decade later. In *Theory and Applications of Computational Chemistry: the first forty years*, Dykstra, C. E.; Frenking, G.; Kim, K. S.; Scueseria, G. E., Eds. Elsevier: Amsterdam, 2005; pp 1167-1189.
33. Fu, Z. W.; Lemire, G. W.; Bishea, G. A.; Morse, M. D., SPECTROSCOPY AND ELECTRONIC-STRUCTURE OF JET-COOLED AL-2. *J. Chem. Phys.* **1990,** *93* (12), 8420-8441.
34. NIST Computational Chemistry Comparison and Benchmark Database. http://cccbdb.nist.gov/.
35. Huber, K.; Herzberg, G., *Constants of Diatomic Molecules*. Van Nostrand Reinhold: New York, 1975.
36. Chase, M. W.; Davies, C. A.; Downey, J. R.; Frurip, D. J.; McDonald, R. A.; Syverud, A. N., JANAF THERMOCHEMICAL TABLES - 3RD EDITION .1. AL-CO. *J. Phys. Chem. Ref. Data* **1985,** *14*, 1-926.

37. Lindsay, C. M. *AFOSR Laboratory Task Report, 17RQCOR451, "Elucidating the phenomena that govern reaction dynamics in assembled nanostructured energetic materials at scales relevant to munitions and propellants"*; 17RQCOR451; Reporting Period 1 Oct 2017-30 Sep 2018.
38. Buszek, R. J.; Ridge, C. J.; Emery, S. B.; Lindsay, C. M.; Boatz, J. A., Theoretical Study of Cu/Mg Core-shell Nanocluster Formation. *J. Phys. Chem. A* **2016,** *120* (48), 9612-9617.
39. Emery, S. B.; Xin, Y.; Ridge, C. J.; Buszek, R. J.; Boatz, J. A.; Boyle, J. M.; Little, B. K.; Lindsay, C. M., Unusual behavior in magnesium-copper cluster matter produced by helium droplet mediated deposition. *J. Chem. Phys.* **2015,** *142* (8).
40. Emery, S. B.; Rider, K. B.; Lindsay, C. M., Stabilized Magnesium/ Perfluoropolyether Nanocomposite Films by Helium Droplet Cluster Assembly. *Propellants Explos. Pyrotech.* **2014,** *39* (2), 161-165.
41. Foley, T. J.; Johnson, C. E.; Higa, K. T., Inhibition of oxide formation on aluminum nanoparticles by transition metal coating. *Chem. Mat.* **2005,** *17* (16), 4086-4091.
42. Jarrold, M. F.; Bower, J. E., THE REACTIONS OF MASS SELECTED ALUMINUM CLUSTER IONS, AL-4-25+ WITH OXYGEN. *J. Chem. Phys.* **1986,** *85* (9), 5373-5375.
43. Fuke, K.; Nonose, S.; Kikuchi, N.; Kaya, K., REACTION OF ALUMINUM CLUSTERS, AL-7-24, WITH OXYGEN AND AMMONIA. *Chem. Phys. Lett.* **1988,** *147* (5), 479-483.
44. Reber, A. C.; Khanna, S. N.; Roach, P. J.; Woodward, W. H.; Castleman, A. W., Spin accommodation and reactivity of aluminum based clusters with O-2. *J. Am. Chem. Soc.* **2007,** *129* (51), 16098-16101.
45. Vogel, H., BETTER WAY TO CONSTRUCT THE SUNFLOWER HEAD. *Mathematical Biosciences* **1979,** *44* (3-4), 179-182.
46. Olsen, J.; Yeager, D. L.; Jorgensen, P., OPTIMIZATION AND CHARACTERIZATION OF A MULTICONFIGURATIONAL SELF-CONSISTENT FIELD (MCSCF) STATE. *Advances in Chemical Physics* **1983,** *54*, 1-176.
47. Shepard, R., *Advances in Chemical Physics* **1987,** *69*, 63-200.
48. Werner, H. J., *Advances in Chemical Physics* **1987,** *69*, 1-62.
49. Dunning, T. H., GAUSSIAN-BASIS SETS FOR USE IN CORRELATED MOLECULAR CALCULATIONS .1. THE ATOMS BORON THROUGH NEON AND HYDROGEN. *J. Chem. Phys.* **1989,** *90* (2), 1007-1023.
50. Kendall, R. A.; Dunning, T. H.; Harrison, R. J., ELECTRON-AFFINITIES OF THE 1ST-ROW ATOMS REVISITED - SYSTEMATIC BASIS-SETS AND WAVE-FUNCTIONS. *J. Chem. Phys.* **1992,** *96* (9), 6796-6806.
51. Hirao, K., STATE-SPECIFIC MULTIREFERENCE MOLLER-PLESSET PERTURBATION TREATMENT FOR SINGLET AND TRIPLET EXCITED-STATES, IONIZED STATES AND ELECTRON ATTACHED STATES OF H2O. *Chem. Phys. Lett.* **1993,** *201* (1-4), 59-66.
52. Hirao, K., MULTIREFERENCE MOLLER-PLESSET PERTURBATION-THEORY FOR HIGH-SPIN OPEN-SHELL SYSTEMS. *Chem. Phys. Lett.* **1992,** *196* (5), 397-403.
53. Hirao, K., MULTIREFERENCE MOLLER-PLESSET PERTURBATION TREATMENT OF POTENTIAL-ENERGY CURVE OF N2. *International Journal of Quantum Chemistry* **1992**, 517-526.
54. Hirao, K., MULTIREFERENCE MOLLER-PLESSET METHOD. *Chem. Phys. Lett.* **1992,** *190* (3-4), 374-380.
55. Zielger, J. F.; Biersack, J. P.; Littmark, U., *The Stopping and Range of Ions in Solids*. Pergamon Press: New York, 1985.
56. Su, J. T.-l. An Electron Force Field for Simulating Large Scale Excited Electron Dynamics. Califronia Institute of Technology, 2007.
57. Zavitsas, A. A., The relation between bond lengths and dissociation energies of carbon-carbon bonds. *J. Phys. Chem. A* **2003,** *107* (6), 897-898.